Double photoionization of aligned molecular hydrogen

W. Vanroose,[1] D. A. Horner,[2] F. Martín,[3] T. N. Rescigno,[2] and C. W. McCurdy[2,4]

[1]*Departement Computerwetenschappen, Katholieke Universiteit Leuven, B-3001 Heverlee, Belgium*
[2]*Lawrence Berkeley National Laboratory, Chemical Sciences, Berkeley, California 94720, USA*
[3]*Departamento de Química C-9, Universidad Autónoma de Madrid, 28049 Madrid, Spain*
[4]*Departments of Applied Science and Chemistry, University of California, Davis, California 95616, USA*
(Received 21 July 2006; published 2 November 2006)

We present converged, completely *ab initio* calculations of the triple differential cross sections for double photoionization of aligned H_2 molecules for a photon energy of 75.0 eV. The method of exterior complex scaling, implemented with both the discrete variable representation and *B*-splines, is used to solve the Schrödinger equation for a correlated continuum wave function corresponding to a single photon having been absorbed by a correlated initial state. Results for a fixed internuclear distance are compared to recent experiments and show that integration over experimental angular and energy resolutions is necessary to produce good qualitative agreement, but does not eliminate some discrepancies. Limitations of current experimental resolution are shown to sometimes obscure interesting details of the cross section.

I. INTRODUCTION

Double photoionization (DPI) is a process in which two electrons are ejected from an atom or molecule as the result of absorption of a single photon. Since the process is controlled by the dipole operator, which is a one-body operator, it cannot be accurately treated with an independent particle description of the target or the final-state dynamics. For that reason, double photoionization represents a powerful way to probe electron correlation. The problem has been extensively investigated, both experimentally and theoretically, for the case of helium. For the simplest two-electron molecule H_2, DPI is followed by a "Coulomb explosion" of the resulting two bare protons. Since this latter process is generally rapid compared to molecular rotation, the relative momentum vector of the dissociating nuclei defines the alignment of the molecule at the instant of photon absorption and allows one to measure differential ionization cross sections of "fixed-in-space" molecules, provided all four charged particles that emerge from the process are measured in coincidence. The advent of "momentum imaging" detectors has made measurements of this type feasible and several experiments on DPI of aligned molecular hydrogen have recently been reported [1–4]. The interpretation of such detailed data pose a significant challenge to *ab initio* theory.

In the double photoionization of helium, the manifestation of dipole selection rules and the patterns observed in the triple differential cross sections (TDCS) are now well understood [5–10]. The degree to which such selection rules survive in the molecular case has been previously discussed [11]. Some proposals, based on the use of approximate wave functions, about the kinds of behaviors that occur in the molecular case have appeared [12], along with proposed atomic-clike model calculations [13] and approximate parametrizations of the entire TDCS using models based on the atomic case [14]. When averaged over molecular orientations, the TDCS patterns for molecular hydrogen are very similar to those for helium [15] and the model calculations work rather well in describing that behavior. However, the TDCS reported for aligned H_2 reveal striking effects of an entirely molecular nature, such as pronounced changes in the patterns of electron ejection that depend on both the orientation of the molecular axis with respect to the photon polarization as well as molecular bond distance. Simple models fail to explain these effects completely and precise quantum theoretical treatments are required to unambiguously unravel the origin of the effects observed.

The initial steps toward a precise quantum solution of the molecular problem were taken a few years ago using grid-based time-dependent close-coupling [16] and exterior complex scaling (ECS) approaches [17]. These initial studies only produced integral cross sections. We have since extended the ECS approach to the computation of TDCS for double photoionization of aligned H_2, and the first results of this treatment were recently announced [18]. In this paper we give a detailed description of the computational procedures employed, present a comprehensive set of numerical results, and compare the results to available experiment.

The outline of this paper is as follows. The theoretical formulation is given in Sec. II. Section II A reviews the ECS approach and presents the first-order equation for the scattered wave that describes double photoionization. We also derive an expression for the DPI amplitude and the molecular distorted waves needed in its evaluation. In Sec. II B we give definitions of the TDCS in terms of the integral amplitudes, give single-center expansion formulas for the scattered wave and for the continuum H_2^+ distorted waves, as well as working expressions for the single and triple differential DPI cross sections. Section II C discusses our treatment of nuclear motion within the Born-Oppenheimer approximation. In Sec. III we describe the two different numerical implementations of ECS used in this work. We briefly review the use of complex-scaled *B*-splines, as well as the use of our complex-scaled finite-element and discrete variable representation. Section IV details the various tests we have carried out to ensure that the numerical results we are presenting are converged. Section V presents our computed results and Sec. VI shows how the results compare with available experiments. This section also details the averaging over finite

ranges of ejection angles, molecular orientations, and energy sharing that must be performed to be able to compare the calculated results with the measured quantities. Section VII contains our conclusions.

II. FORMULATION OF THE MOLECULAR DOUBLE PHOTOIONIZATION PROBLEM

A. Exterior complex scaling approach

The amplitude for double photoionization is associated with the purely outgoing wave function Ψ_{sc}^+ that is the solution of the driven Schrödinger equation—the so-called "first-order wave function" obtained when we treat the radiation field as a perturbation. That equation can be written in the "velocity form" for a two-electron problem using atomic units ($\hbar = m_e = e = 1$) as

$$(E_0 + \omega - H)|\Psi_{sc}^+\rangle = \boldsymbol{\epsilon} \cdot (\boldsymbol{\nabla}_1 + \boldsymbol{\nabla}_2)|\Psi_0\rangle \quad (1)$$

where $\boldsymbol{\epsilon}$ is the polarization unit vector, $\boldsymbol{\nabla}_1$ and $\boldsymbol{\nabla}_2$ are the gradient operators for the electronic coordinates, and $|\Psi_0\rangle$ is the initial (bound) state of the target. The key difficulty in double photoionization calculations is the application of proper outgoing wave scattering boundary conditions on Ψ_{sc}^+ for the three-body Coulomb breakup problem.

Those boundary conditions can be applied rigorously, as discussed in a recent review [19], by transforming the radial coordinates of both electrons according to the ECS transformation [20,21] which scales those coordinates by a complex factor, $\exp(i\eta)$ beyond some radius R_0, as shown in Fig. 1

$$r \rightarrow \begin{cases} r, & r \leq R_0 \\ R_0 + (r - R_0)e^{i\eta}, & r > R_0 \end{cases} \quad (2)$$

and requiring $\Psi_{sc}^+(\mathbf{r}_1, \mathbf{r}_2) \rightarrow 0$ when either of the electronic coordinates goes to infinity. The reason is that applying the ECS transformation to the electronic radial coordinates in Eq. (1) causes all purely outgoing solutions, regardless of the number of electrons in the continuum, to decay exponentially for any $r_i > R_0$.

Solving Eq. (1) for the first-order wave function in this manner, with R_0 having been chosen large enough to allow $\Psi_{sc}^+(\mathbf{r}_1, \mathbf{r}_2)$ to reach its asymptotic form where both coordinates are real valued, provides us with the physical wave function in the region where both coordinates are less than R_0. We are thus faced with the problem of extracting the double photoionization amplitude from a wave function we only know on a finite volume. A procedure for doing so for the case of atomic double photoionization (or electron-impact ionization) is now well established [10,19,22]. The double photoionization amplitude of the helium atom, for example, can be given as a volume integral involving Ψ_{sc}^+ and a pair of distorted waves or "testing functions,"

$$f(\mathbf{k}_1, \mathbf{k}_2) = \langle \Phi_c^{(-)}(\mathbf{k}_1, \mathbf{r}_1)\Phi_c^{(-)}(\mathbf{k}_2, \mathbf{r}_2)|E - T - V_1|\Psi_{sc}^+\rangle, \quad (3)$$

where E is the total energy, T is the two-electron kinetic energy operator, and V_1 is the sum of all one-electron potentials for the atom
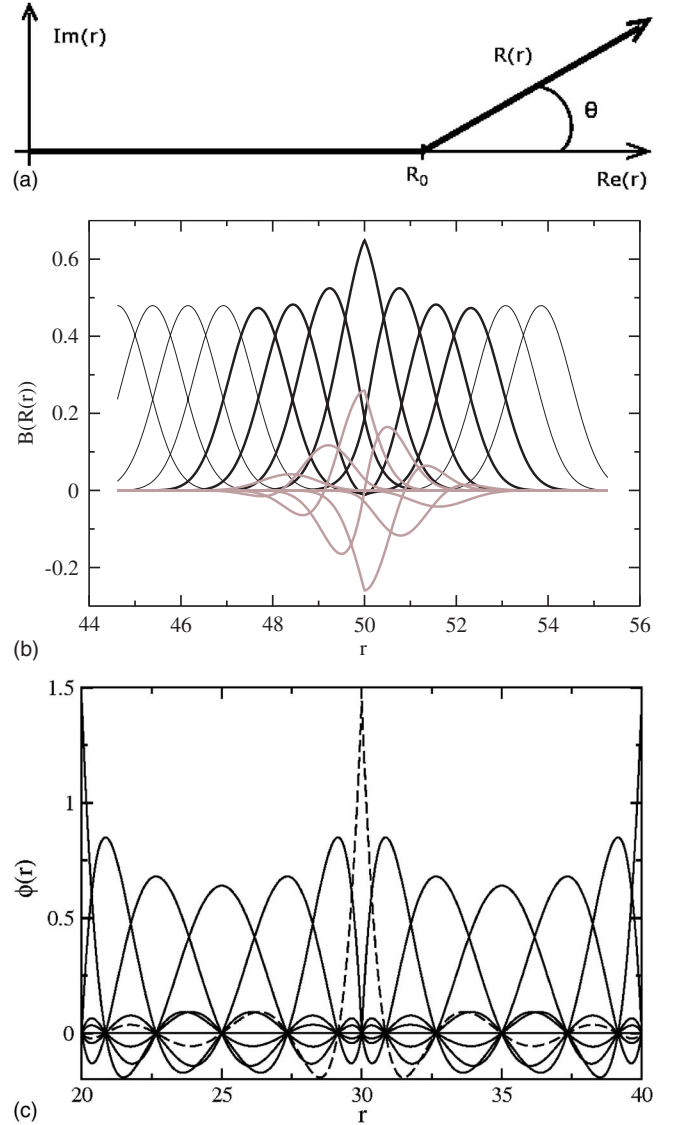

FIG. 1. (Color online) Exterior complex scaling in a single radial dimension. (a) ECS contour in the complex plane. (b) Eighth-order B-splines on the ECS contour with $R_0 = 50$ and a scaling angle of 40°; thin lines are real B-splines and heavy dark and light lines are real and imaginary parts, respectively, of complex B-splines. (c) Seventh-order FEM/DVR functions plotted over two elements; the dashed curve is the central bridging function which connects the basis functions in the two adjacent elements.

$$V_1 = -Z/r_1 - Z/r_2. \quad (4)$$

The $\Phi_c^{(-)}(\mathbf{k}, \mathbf{r})$ are Coulomb functions normalized to a delta function in momentum and with effective charge Z. The integral in Eq. (3) can be performed over the finite volume enclosed by the radius R_0 and has been shown to produce the physical breakup amplitude aside from a knowable, but irrelevant, overall phase [19,23]. While formally we may choose any charges for the testing functions and the potential V_1 in Eq. (4), the choice of $Z = 2$ causes them to be orthogonal to the bound states of He$^+$, thereby removing any contribution to the integral in Eq. (3) from single ionization that leaves

the ion in any state that is effectively contained within R_0. With this amplitude $f(\mathbf{k}_1, \mathbf{k}_2)$ in hand, the TDCS cross section for double photoionization of a two electron atom is given by

$$\frac{d^3\sigma}{dE_1 d\Omega_1 d\Omega_2} = \frac{4\pi^2}{\omega c} k_1 k_2 |f(\mathbf{k}_1, \mathbf{k}_2)|^2. \tag{5}$$

B. The molecular double photoionization amplitude

1. The amplitude integral

To calculate the TDCS for double photoionization of H_2 we require the molecular analog of Eq. (3). That expression is, for a fixed internuclear distance,

$$f(\mathbf{k}_1, \mathbf{k}_2) = \langle \Phi^{(-)}(\mathbf{k}_1, \mathbf{r}_1) \Phi^{(-)}(\mathbf{k}_2, \mathbf{r}_2) |$$
$$\times [E - T - v(\mathbf{r}_1) - v(\mathbf{r}_2)] |\Psi_{sc}^+(\mathbf{r}_1, \mathbf{r}_2)\rangle, \tag{6}$$

where E is the excess energy above the double ionization threshold, T is the two-electron kinetic energy operator, and $v(r)$ is the nuclear attraction potential seen by one electron in the field of the bare nuclei. The functions $\Phi^{(-)}(\mathbf{k}, \mathbf{r})$ are thus H_2^+ continuum eigenfunctions with incoming momentum $\mathbf{k}$. While there are other choices of testing functions that are formally equivalent, this choice is optimal for our purposes because the orthogonality of the H_2^+ continuum eigenfunctions to the bound states of H_2^+ eliminates the contributions of the single ionization channels to Eq. (6) in the same way that the choice of $Z=2$ Coulomb functions does so for the case of helium. It must be emphasized again that the product of testing functions is *not* the physical final-state wave function. The physical final state for double ionization is contained in the function Ψ_{sc}^+. As discussed previously [19], this integral expression merely extracts the amplitude for double ionization from Ψ_{sc}^+.

2. H_2^+ continuum functions

For the molecular case, even the one-electron testing functions in Eq. (6) pose a computational challenge. They are continuum states of the H_2^+ ion in the Born-Oppenheimer approximation where the electron leaves behind two bare protons, positioned at $\pm\mathbf{A}$. Thus the one-electron testing functions $\Phi^{(-)}$ we must use in this case are solutions of

$$\left[\frac{k^2}{2} + \frac{\nabla^2}{2} + \frac{1}{|\mathbf{r} - \mathbf{A}|} + \frac{1}{|\mathbf{r} + \mathbf{A}|} \right] \Phi^{(-)}(\mathbf{k}, \mathbf{r}) = 0, \tag{7}$$

and satisfy the usual relation, $\Phi^{(-)}(\mathbf{k}, \mathbf{r}) = [\Phi^{(+)}(-\mathbf{k}, \mathbf{r})]^*$. Our goal is to define a procedure for evaluating Eq. (6) to arbitrary accuracy, thereby producing an effectively exact value of the fixed-nuclei double photoionization amplitude within the Born-Oppenheimer approximation. We therefore require a procedure for exactly calculating the continuum wave functions of H_2^+.

To do so we convert Eq. (7) into a driven equation for the scattered wave part of $\Phi^{(+)}$. Because the incoming wave part of the solution is determined by the long range behavior of the potential in Eq. (7) it is the same as that of the atomic

Coulomb problem with $Z=2$. Therefore we can write the H_2^+ wave function as

$$\Phi^{(+)}(\mathbf{k}, \mathbf{r}) = \chi(\mathbf{k}, \mathbf{r}) + \Phi_c^{(+)}(\mathbf{k}, \mathbf{r}) \tag{8}$$

with the "unperturbed" portion being the standard ($Z=2$) Coulomb function, $\Phi_c^{(+)}(\mathbf{k}, \mathbf{r})$, whose incoming momentum specifies the direction of $\mathbf{k}$. The scattered wave portion $\chi(\mathbf{k}, \mathbf{r})$ of the exact H_2^+ continuum function then satisfies the driven Schrödinger equation

$$\left(\frac{k^2}{2} - h \right) \chi(\mathbf{k}, \mathbf{r}) = \left(h - \frac{k^2}{2} \right) \Phi_c^{(+)}(\mathbf{k}, \mathbf{r})$$

$$= \left(\frac{2}{r} - \frac{1}{|\mathbf{r} - \mathbf{A}|} - \frac{1}{|\mathbf{r} + \mathbf{A}|} \right) \Phi_c^{(+)}(\mathbf{k}, \mathbf{r}) \tag{9}$$

with h being the one-electron Hamiltonian in Eq. (7). Since χ is an outgoing wave, the correct boundary conditions can be imposed using the ECS transformation as described above.

We require the solution of Eq. (9) for any direction of the momentum in $\Phi_c^{(+)}(\mathbf{k}, \mathbf{r})$. In the body-fixed frame we can write that solution as a single-center expansion of the form

$$\Phi^+(\mathbf{k}, \mathbf{r}) = \sum_{l,m,l'} \varphi_{ll'm}(r, k) Y^*_{lm}(\hat{\mathbf{k}}) Y_{l'm}(\hat{\mathbf{r}}), \tag{10}$$

where we have made use of the fact that m is a good quantum number. To construct the effective radial functions $\varphi_{ll'm}(r, k)$ we need to make the appropriate single-center expansion of the quantities in Eq. (8). First, we write the standard expansion of the momentum normalized Coulomb function

$$\Phi_c^{(+)}(\mathbf{k}, \mathbf{r}) = \left(\frac{2}{\pi} \right)^{1/2} \sum_{l,m} \frac{i^l e^{i\eta_l(k)}}{kr} \phi_{l,k}^{(c)}(r) Y_{lm}(\hat{\mathbf{r}}) Y^*_{lm}(\hat{\mathbf{k}}), \tag{11}$$

where $\phi_{l,k}^{(c)}(r)$ is the radial Coulomb function with asymptotic form $\sin[kr + (Z/k)\ln 2kr - l\pi/2 + \eta_l(k)]$, and the Coulomb phase is

$$\eta_l(k) = \arg \Gamma(l + 1 - iZ/k). \tag{12}$$

We can then define a set of solutions of the driven Schrödinger equation with right-hand sides proportional to an incident Coulomb function with a single $Y_{l_0 m_0}$

$$(E - h)\chi^{l_0, m_0}(\mathbf{r}) = (h - E) \frac{\phi_{l_0, k}^{(c)}(r)}{kr} Y_{l_0, m_0}(\hat{\mathbf{r}}). \tag{13}$$

Next, we make a single-center expansion of the function $\chi^{l_0, m_0}(\mathbf{r})$,

$$\chi^{l_0, m_0}(\mathbf{r}) = \sum_l \frac{R_l^{l_0 m_0}(r)}{r} Y_{lm_0}(\hat{\mathbf{r}}), \tag{14}$$

of course choosing the z axis to coincide with $\hat{\mathbf{A}}$, and using the fact that m is a good quantum number. The result is a set of coupled equations for the outgoing radial functions $R_l^{l_0 m_0}$ corresponding to an incident Coulomb wave with angular momentum quantum numbers l_0 and m_0, that must be solved for every l_0 and m_0 that we are considering in the expansion basis:

$$\sum_l \left\{ \delta_{l',l} \left[E - \left(-\frac{1}{2} \frac{d^2}{dr^2} + \frac{l(l+1)}{2r^2} \right) \right] - v_{l',l}^{m_0}(r) \right\} R_l^{l_0 m_0}(r)$$

$$= \left[v_{l',l_0}^{m_0}(r) + \frac{2}{r} \delta_{l',l_0} \right] \frac{1}{k} \phi_{l_0,k}^{(c)}(r), \tag{15}$$

where

$$v_{l',l}^{m_0}(r) = \int d\hat{\mathbf{r}} \, Y_{l' m_0}^*(\hat{\mathbf{r}}) \left(-\frac{1}{|\mathbf{r} - \mathbf{A}|} - \frac{1}{|\mathbf{r} + \mathbf{A}|} \right) Y_{l m_0}(\hat{\mathbf{r}}). \tag{16}$$

However, since parity is conserved the sum Σ_l is restricted to even (odd) values if l_0 is even (odd).

The complete solution of Eq. (9) can be constructed for any direction of $\mathbf{k}$ as a linear combination of the solutions of Eq. (15),

$$\chi(\mathbf{k}, \mathbf{r}) = \sum_{l_0, m_0} i^{l_0} e^{i \eta_{l_0}(k)} Y_{l_0, m_0}^*(\hat{\mathbf{k}}) \chi^{l_0, m_0}(\mathbf{r})$$

$$= \sum_{l, l_0, m_0} i^{l_0} e^{i \eta_{l_0}(k)} Y_{l_0, m_0}^*(\hat{\mathbf{k}}) \frac{R_l^{l_0 m_0}(r)}{r} Y_{l m_0}(\hat{\mathbf{r}}). \tag{17}$$

The resulting single-center expansion of the H_2^+ scattering eigenstates in the body-fixed frame is thus

$$\Phi^{(+)}(\mathbf{k}, \mathbf{r}) = \left(\frac{2}{\pi} \right)^{1/2} \sum_{l,m} i^l e^{i \eta_l(k)} Y_{lm}^*(\hat{\mathbf{k}})$$

$$\times \sum_{l'} \Delta_{l,l'} \left(\frac{\phi_{l,k}^{(c)}(r)}{kr} \delta_{l,l'} + \frac{R_{l'}^{lm}}{r} \right) Y_{l'm}(\hat{\mathbf{r}}), \tag{18}$$

and has the form of Eq. (10). In Eq. (18) the factor $\Delta_{l,l'}$ is unity if $l+l'$ is even and zero otherwise. The first sum ranges over the values of l and m for the incident waves, while the second sum is over the outgoing waves with l' for a particular l and m of the incident wave. As described below in Sec. III, we can construct the radial functions $R_{l'}^{lm}(r)$ by expanding them in a basis of discrete functions, and substituting that representation back into Eq. (15) to obtain linear equations for their coefficients.

3. The partial-wave double ionization amplitudes

With the one-electron continuum states of H_2^+ in hand, we turn to the calculation of the two-electron continuum function, Ψ_{sc}^+, in Eq. (1). We can write that wave function, for a fixed value of the projection M of the electronic angular momentum along the molecular axis and for singlet spin coupling, as a sum of products of two-dimensional radial wave functions and spherical harmonics

$$\Psi_{\text{sc}}^{+(M)} = \sum_{\mu_1 \mu_2, j_1 \geq j_2} \left(\frac{\psi_{j_1 \mu_1, j_2 \mu_2}^{\text{dir}}(r_1, r_2)}{r_1 r_2} Y_{j_1 \mu_1}(\hat{\mathbf{r}}_1) Y_{j_2 \mu_2}(\hat{\mathbf{r}}_2) \right.$$

$$\left. + \frac{\psi_{j_1 \mu_1, j_2 \mu_2}^{\text{exch}}(r_1, r_2)}{r_1 r_2} Y_{j_2 \mu_2}(\hat{\mathbf{r}}_1) Y_{j_1 \mu_1}(\hat{\mathbf{r}}_2) \right). \tag{19}$$

In Eq. (19) we have partitioned the wave function into direct

and exchange components by employing an explicitly symmetrized representation for singlet spin coupling, but we should point out that it would also be possible to use an unsymmetrized representation with sums over j_1 and j_2 unrestricted except by parity. In the case that Ψ_0 is the $^1\Sigma_g^+$ ground state of H_2, the outgoing state Ψ_{sc}^+ can have only $^1\Sigma_u^+$ ($M=0$) or $^1\Pi_u$ ($M=\pm1$) symmetry. Thus, for the case at hand, if j_1 is even j_2 must be odd and vice versa to produce ungerade symmetry in Ψ_{sc}^+, significantly reducing the size of the computations. The radial functions $\psi_{j_1 \mu_1, j_2 \mu_2}^{\text{dir}}(r_1, r_2)$ and $\psi_{j_1 \mu_1, j_2 \mu_2}^{\text{exch}}(r_1, r_2)$ are then expanded in products of B-splines or of discrete variable representation (DVR) basis functions, so that the Hamiltonian matrix elements corresponding to the lhs of Eq. (1) are the same as those in a "complete configuration interaction" calculation in that basis.

The amplitude for double ionization expressed as a six-dimensional volume integral in Eq. (6) can be recast using Gauss' theorem as a five-dimensional surface integral on a sphere of constant ρ in hyperspherical coordinates,

$$f(\mathbf{k}_1, \mathbf{k}_2) = \int d\Omega_1 \int d\Omega_2 \int d\rho \int_0^{\pi/2} d\alpha \frac{\rho^5 \sin^2\alpha \cos^2\alpha}{2}$$

$$\times \Phi^{(-)}(\mathbf{k}_1, \mathbf{r}_1)^* \Phi^{(-)}(\mathbf{k}_2, \mathbf{r}_2)^*$$

$$\times \left[\frac{\overleftarrow{\partial}}{\partial \rho} \delta(\rho - \rho_0) - \delta(\rho - \rho_0) \frac{\overrightarrow{\partial}}{\partial \rho} \right] \Psi_{\text{sc}}^+(\mathbf{r}_1, \mathbf{r}_2), \tag{20}$$

where the notation of the partial derivatives with respect to the hyper-radius means that they operate to the left and right as indicated and the delta functions constrain the integration to the surface of the hypersphere. The hyperspherical coordinates are $\rho = \sqrt{r_1^2 + r_2^2}$ and $\tan \alpha = r_2/r_1$, in addition to the normal spherical polar angles we have denoted Ω_1 and Ω_2. This surface integral is written in a form that allows us to make direct use of the radial functions from calculations performed in ordinary spherical coordinates, instead of the more familiar hyperradial functions [24] of ρ in this coordinate system.

We can now substitute the partial-wave expansions of the two one-electron test functions $\Phi^{(-)}(\mathbf{k}_1, \mathbf{r}_1)$ and $\Phi^{(-)}(\mathbf{k}_2, \mathbf{r}_2)$ [given by $\Phi^{(+)}(-\mathbf{k}, \mathbf{r})^*$] and the two-electron wave function of Eq. (19) into the surface integral expression for the amplitude in Eq. (20). Integrating over $d\Omega_1$ and $d\Omega_2$ yields an expression for the double ionization amplitude for a particular value of M. Because of the orthogonality of the spherical harmonics, the integration over angles Ω_1 and Ω_2 connects outgoing waves of the two-electron wave function with a particular $Y_{j_1 \mu_1}(\hat{\mathbf{r}}_1) Y_{j_2 \mu_2}(\hat{\mathbf{r}}_2)$ to the corresponding components of the two one-electron test functions,

$$f^{(M)}(\mathbf{k}_1, \mathbf{k}_2)$$

$$= \sum_{l_1, \mu_1} \sum_{l_2, \mu_2} \left(\frac{2}{\pi} \right) i^{-l_1 - l_2} e^{i \eta_{l_1}(k_1) + i \eta_{l_2}(k_2)}$$

$$\times \left[Y_{l_1 \mu_1}(\hat{\mathbf{k}}_1) Y_{l_2 \mu_2}(\hat{\mathbf{k}}_2) \sum_{j_1 \geq j_2} F_{l_1 l_2 j_1 j_2 \mu_1 \mu_2}^{\text{dir}}(k_1, k_2) \Delta_{j_1 l_1} \Delta_{j_2 l_2} \right.$$

$$+ Y_{l_1\mu_2}(\hat{\mathbf{k}}_1)Y_{l_2\mu_1}(\hat{\mathbf{k}}_2)\sum_{j_1\gtrless j_2}F^{\text{exch}}_{l_1l_2j_1\mu_1j_2\mu_2}(k_1,k_2)\Delta_{j_2l_1}\Delta_{j_1l_2}\Bigg],$$
(21)

where $M=\mu_1+\mu_2$, and again, the factor $\Delta_{j,l}$ is unity if $j+l$ is even and zero otherwise. The direct radial amplitude in this expression is the surface integral for particular angular components,

$$F^{\text{dir}}_{l_1,l_2,j_1,\mu_1,j_2,\mu_2}(k_1,k_2)$$

$$= \frac{\rho_0}{2}\int_0^{\pi/2}d\alpha\left(\frac{\phi^{(c)}_{l_1,k_1}(r_1)}{k_1}\delta_{l_1,j_1}+R^{l_1\mu_1}_{j_1}(r_1)\right)$$

$$\times\left(\frac{\phi^{(c)}_{l_2,k_2}(r_2)}{k_2}\delta_{l_2,j_2}+R^{l_2\mu_2}_{j_2}(r_2)\right)$$

$$\times\left[\frac{\overleftarrow{\partial}}{\partial\rho}-\frac{\overrightarrow{\partial}}{\partial\rho}\right]_{\rho=\rho_0}\psi^{\text{dir}}_{j_1\mu_1j_2\mu_2}(r_1,r_2),$$
(22)

and the corresponding exchange amplitude can be gotten from this expression by interchanging j_1,μ_1 and j_2,μ_2 on the rhs in the test functions (but not in the wave function, $\psi^{\text{exch}}_{j_1\mu_1j_2\mu_2}$). Further details about the relation between direct and exchange amplitudes are contained in the Appendix. Each two-electron radial function corresponding to a particular angular component $Y_{j_1\mu_1}(\hat{\mathbf{r}}_1)Y_{j_2\mu_2}(\hat{\mathbf{r}}_2)$ produces a set of these direct (or exchange amplitudes). This is true because a number of radial one-electron test functions with values l_1 and l_2 for their incident Coulomb waves can have outgoing waves with angular momenta $j_1\mu_1$ and $j_2\mu_2$.

We can simplify the expression in Eq. (21) by performing the sums over the angular momenta j_1 and j_2 that are associated with the single-center expansion of $\Psi^{+(M)}_{\text{sc}}$ and thereby defining "reduced amplitudes," $\mathcal{F}^{\text{dir,exch}(M)}_{l_1,l_2,\mu_1,\mu_2}(k_1,k_2)$

$$f^{(M)}(\mathbf{k}_1,\mathbf{k}_2)=\sum_{l_1,\mu_1}\sum_{l_2,\mu_2}\left(\frac{2}{\pi}\right)i^{-l_1-l_2}e^{i\eta_{l_1}(k_1)+i\eta_{l_2}(k_2)}$$

$$\times[\mathcal{F}^{\text{dir}(M)}_{l_1,l_2,\mu_1,\mu_2}(k_1,k_2)Y_{l_1\mu_1}(\hat{\mathbf{k}}_1)Y_{l_2\mu_2}(\hat{\mathbf{k}}_2)$$

$$+\mathcal{F}^{\text{exch}(M)}_{l_1,l_2,\mu_1,\mu_2}(k_1,k_2)Y_{l_1\mu_2}(\hat{\mathbf{k}}_1)Y_{l_2\mu_1}(\hat{\mathbf{k}}_2)].$$
(23)

Note that with this notation only one of the two reduced amplitudes, $\mathcal{F}^{\text{dir,exch}(M)}_{l_1,l_2,\mu_1,\mu_2}(k_1,k_2)$, is nonzero in each term of these sums.

To construct the TDCS for arbitrary orientations of the polarization vector relative to the axis of the molecule in the body-fixed frame, we require the amplitudes for all three values of M. For a given direction of the polarization vector, a convenient working expression for the double ionization amplitude for a given direction of the polarization vector, $\hat{\epsilon}=(\hat{\epsilon}_x,\hat{\epsilon}_y,\hat{\epsilon}_z)$, in the body fixed frame, is

$$f(\mathbf{k}_1,\mathbf{k}_2,\hat{\epsilon})=\frac{(\hat{\epsilon}_x+i\hat{\epsilon}_y)}{\sqrt{2}}f^{(-1)}(\mathbf{k}_1,\mathbf{k}_2)+\hat{\epsilon}_zf^{(0)}(\mathbf{k}_1,\mathbf{k}_2)$$

$$+\frac{(-\hat{\epsilon}_x+i\hat{\epsilon}_y)}{\sqrt{2}}f^{(+1)}(\mathbf{k}_1,\mathbf{k}_2),$$
(24)

where the amplitudes $f^{(M)}$, defined by Eq. (21) or (23), are constructed from the solutions of Eq. (1) for $M=(0,\pm 1)$ with the appropriate spherical component of the dipole operator in the driving term. In the length representation those components of the dipole operator are $\mu_M=[r_1\sqrt{4\pi/3}Y_{1,M}(\Omega_1)+r_2\sqrt{4\pi/3}Y_{1,M}(\Omega_2)]$. The corresponding operator components in the velocity form, in which Eq. (1) is written, are given by Rose [25]. Note that the Cartesian components of the polarization vector are expressed here in the molecule-fixed coordinate system with the internuclear axis as the z axis.

The single differential cross section (SDCS) can be expressed in a way that closely resembles the atomic case [10] by using the reduced amplitudes $\mathcal{F}$ defined in Eq. (23) whose indices label the incoming waves of the H_2^+ continuum functions:

$$\frac{d\sigma^{(M)}}{dE_1}=\frac{4\pi^2}{\omega c}k_1k_2\left(\frac{2}{\pi}\right)^2\sum_{l_1>l_2,\mu_1,\mu_2}[|\mathcal{F}^{\text{dir}(M)}_{l_1,l_2,\mu_1,\mu_2}(k_1,k_2)|^2$$

$$+|\mathcal{F}^{\text{exch}(M)}_{l_1,l_2,\mu_1,\mu_2}(k_1,k_2)|^2],$$
(25)

where we have taken advantage of homonuclear symmetry and the fact that $l_1\neq l_2$ to restrict the sum over those indices. For linearly polarized incident radiation and randomly oriented molecules the physical SDCS has contributions from all three M values, and we can write it in the form

$$\frac{d\sigma}{dE_1}=\frac{1}{3}\left(\frac{d\sigma^{(\Sigma)}}{dE_1}+2\frac{d\sigma^{(\Pi)}}{dE_1}\right).$$
(26)

The integral cross section is the integral of this SDCS from 0 to E, the energy of the photon above the double photoionization threshold.

C. Born-Oppenheimer approximation

In deriving an expression for the double photoionization amplitude, we have implicitly made use of the Born-Oppenheimer approximation to separate electronic and nuclear motion. Thus the ionization amplitude $f(\mathbf{k}_1,\mathbf{k}_2;R)$ is an electronic quantity that depends parametrically on the internuclear separation R. The experimentally observed quantity however is not R, but rather the nuclear kinetic energy release (KER), or equivalently, by energy conservation, the sum of the kinetic energies of the ejected electrons. So the next task is to see how the TDCS corresponding to specific values of KER are computed from the fixed-nuclei amplitudes computed for different values of R.

In the following, we will assume that there is no interaction between vibrational and rotational motion so that the rotational wave functions can be factored out. Moreover, we assume that following photon absorption, the nuclei fly apart along a vector that remains stationary (i.e., does not rotate) in

the laboratory frame. This assumption is known as the *axial recoil approximation* and is certainly valid when the rotational temperature of the target gas is low and the photon energy is well above threshold, which is the case we wish to consider. We further assume the validity of the Born-Oppenheimer approximation, which allows us to factor the total wave functions, both for the initial bound target state and the final continuum state, into products of electronic and vibrational functions. With these assumptions, we can write the ionization amplitude as

$$F_\kappa(\hat{\mathbf{k}}_1, \hat{\mathbf{k}}_2, \hat{\epsilon}) = \int_0^\infty dR\, \chi_\kappa(R) f(\mathbf{k}_1, \mathbf{k}_2, \hat{\epsilon}; R) \chi_0(R), \quad (27)$$

where κ labels the KER and $\chi_0(R)$ and $\chi_\kappa(R)$ are the initial (bound) and final (energy-normalized continuum) vibrational wave functions, respectively. In the present case, the latter is simply the repulsive Coulomb function corresponding to two bare protons, satisfying

$$\left(-\frac{1}{2\mu}\frac{d^2}{dR^2} + \frac{1}{R} - \frac{\kappa^2}{2\mu}\right)\chi_\kappa(R) = 0. \quad (28)$$

In the context of electron-molecule scattering, where $f(\mathbf{k}_1, \mathbf{k}_2; R)$ would be replaced by a fixed-nuclei T matrix, this treatment is called the *adiabatic nuclei approximation* and Eq. (27) is frequently referred to as Chase's approximation [26].

There is an ambiguity that arises in the adiabatic nuclei approximation concerning the proper choice of electron energy in the fixed-nuclei electronic amplitude, since the latter depends only parametrically on R and has no explicit dependence on target vibrational energies. This can be a problem when trying to compute cross sections near thresholds. In electronically elastic electron-molecule scattering, for example, where the fixed-nuclei amplitude depends on a single energy parameter, there is no unique prescription for choosing the electron energy when treating vibrational excitation [27]. The idea of using an off-shell T matrix in such cases has proven to be a useful expedient [27–29].

In the case of photoabsorption, where free electrons appear only in the final state, there is less ambiguity about how to choose the free-electron energy. In dissociative photoionization, which we are considering here, the fixed-nuclei excitation energy to the dissociative state changes rapidly with internuclear distance, which is a factor that must be accounted for when deciding how to partition the photon energy between the free electrons and the dissociating nuclei. The physical situation is illustrated in Fig. 2, which shows the target potential energy curves for the initial and final states, the associated bound and continuum nuclear wave function and the various energies involved. Formally, for a given photon energy $h\nu$, the observable KER can range from zero to $h\nu + E_o$, where E_o is the initial (negative) target energy, where the zero of energy is chosen as separated electrons *and* nuclei. In practice, the range of detectable KERs, as well as the range of R values required in evaluating the integral in Eq. (27), is determined by the Franck-Condon envelope of the initial vibrational state reflected onto the final dissociative potential curve.
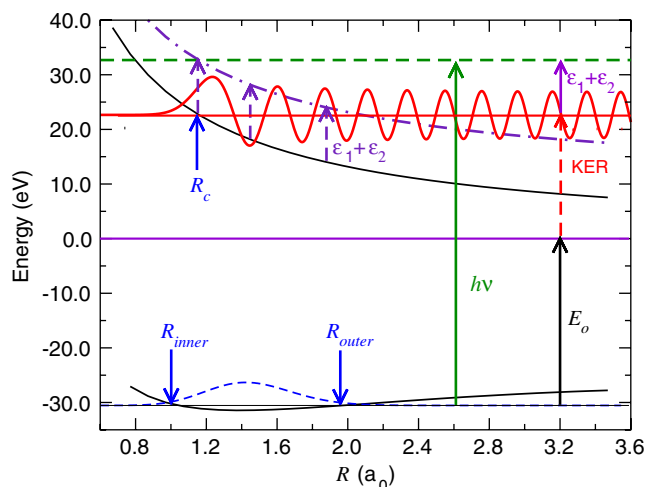

FIG. 2. (Color online) Double photoionization of H_2. The molecule is excited from the $X^1\Sigma_g^+$ state (lower curve) to the double continuum consisting of bare protons (upper curve) and two free electrons with energies ε_1 and ε_2. Also shown are the $v=0$ ground state (dashed) and final (light solid) vibrational wave functions. E_0 is the initial target energy and the upper dashed line indicates the total (target plus photon) energy. The Franck-Condon interval is the range of R values between R_{inner} and R_{outer}. R_c is the classical turning point along the upper potential curve for a specified value of nuclear kinetic energy release (KER). See text for a description of a scheme for evaluating the ionization amplitude in the adiabatic nuclei approximation which involves an integration over R (corresponding to the upper dash-dot curve), in which ε_1 and ε_2 are kept fixed (broken arrows on upper curve).

The kinetic energy release and the photoelectron energies (see Fig. 2) are related by energy conservation:

$$E_0 + h\nu = \varepsilon_1 + \varepsilon_2 + \frac{\kappa^2}{2\mu}. \quad (29)$$

For a fixed photon energy, there is an infinite number of energy sharings between electrons and nuclei that satisfy Eq. (29). Once the KER is specified, the final nuclear continuum state of Eq. (28) and the total photoelectron energy are determined. We must then decide which fixed-nuclei amplitudes to employ in performing the R integral required in Eq. (27). One possibility is to construct, at each value of R, the amplitude for the specified photoelectron energies. This procedure was used by Sánchez and Martín in studying dissociative photoionization of H_2 [30] and by Stibbe and Tennyson [31] in an analogous study of near-threshold electron impact dissociation of H_2.

In the case of double ionization, such a procedure is extremely demanding since the R-dependent amplitudes required in the evaluation of Eq. (27) (corresponding to an integration along the upper dash-dot curve in Fig. 2) must be recalculated for each different value of KER. In our approach we would solve the driven Schrödinger equation

$$[\varepsilon_1 + \varepsilon_2 - H_{\text{elec}}(R)]|\Psi_{\text{sc}}^+(R)\rangle = \boldsymbol{\epsilon} \cdot (\boldsymbol{\nabla}_1 + \boldsymbol{\nabla}_2)|\Psi_0(R)\rangle,$$

(30)

where $H_{\text{elec}}(R)$ is the electronic Hamiltonian. The sum of the electron energies, $\varepsilon_1 + \varepsilon_2$, is determined by Eq. (29) for each value of the KER.

However, in these calculations we have employed a simplifying approximation. We first note that the inner and outer classical turning points of the molecule in its initial vibrational state place effective upper and lower bounds on the observable values of KER. When the photon energy is well above the Franck-Condon threshold, the continuum nuclear wave function $\chi_\kappa(R)$ oscillates rapidly beyond its classical turning point R_c, which will necessarily lie between R_{inner} and R_{outer} over the range of observable KER. In such cases, the R integral in Eq. (27) is well approximated by the method of a stationary phase, the stationary phase point coinciding with the classical turning point R_c. The resulting simplification is that, if χ_κ is an energy-normalized continuum function,

$$\begin{aligned}
F_\kappa(\hat{\mathbf{k}}_1, \hat{\mathbf{k}}_2, \hat{\boldsymbol{\epsilon}}) &= \int_0^\infty dR\, \chi_\kappa(R) f(\mathbf{k}_1, \mathbf{k}_2, \hat{\boldsymbol{\epsilon}}; R) \chi_0(R) \\
&\approx \int_{R_{\text{inner}}}^{R_{\text{outer}}} dR \left| \frac{dV}{dR} \right|^{-1/2} \delta(R - R_c) \\
&\quad \times f(\mathbf{k}_1, \mathbf{k}_2, \hat{\boldsymbol{\epsilon}}; R) \chi_0(R) \\
&= \left| \frac{dV}{dR} \right|_{R=R_c}^{-1/2} f(\mathbf{k}_1, \mathbf{k}_2, \hat{\boldsymbol{\epsilon}}; R_c) \chi_0(R_c).
\end{aligned}$$

(31)

This essentially classical result states that, for purposes of evaluating the integral in Eq. (27), the continuum nuclear wave function can be replaced by a δ function at the classical turning point and thus, in this limit, there is a one-to-one mapping between KER and internuclear distance. We have verified by explicit computational tests that this approximation is well justified for the conditions we are considering here.

With the inclusion of the nuclear degree of freedom we are ready to define the fully differential cross section in the body fixed frame for a particular orientation of the polarization vector relative to the molecular axis,

$$\frac{d^6\sigma}{dE_1 dE_N d\Omega_1 d\Omega_2} = \frac{4\pi^2}{\omega c} k_1 k_2 |F_\kappa(\hat{\mathbf{k}}_1, \hat{\mathbf{k}}_2, \hat{\boldsymbol{\epsilon}})|^2,$$

(32)

where $E_N = \kappa^2/2\mu$, E_1 is the energy of one of the electrons, and the solid angles are for the two electrons. The polarization vector and the directions of the electron momenta are in this expression measured relative to the molecular axis. Rotating the three vectors, $\mathbf{k}_1, \mathbf{k}_2, \hat{\boldsymbol{\epsilon}}$, together around the molecular axis simply rotates the cross section about that axis in this frame.

The dependence of the fixed-nuclei TDCS on internuclear separation along with a detailed treatment of the nuclear dynamics will be explored in a subsequent publication. Since the results we are reporting here are for calculations all carried out at the equilibrium internuclear distance and since we

will be comparing with experimental results integrated over available kinetic energy release, we will make a final simplifying approximation. Substituting the amplitude from Eq. (31) into Eq. (32) and integrating over E_N using $E_N = 1/R_c$ gives

$$\frac{d^5\sigma}{dE_1 d\Omega_1 d\Omega_2} = \frac{4\pi^2}{\omega c} k_1 k_2 \int dR |\chi_0(R) f(\mathbf{k}_1, \mathbf{k}_2, \hat{\boldsymbol{\epsilon}}; R)|^2.$$

(33)

Since $\chi_0(R)$ is strongly peaked about the equilibrium internuclear distance R_{eq}, it is a reasonable approximation to replace $f(\mathbf{k}_1, \mathbf{k}_2, \hat{\boldsymbol{\epsilon}}; R)$ by $f(\mathbf{k}_1, \mathbf{k}_2, \hat{\boldsymbol{\epsilon}}; R_{eq})$ and take it outside the integral in Eq. (33):

$$\begin{aligned}
\frac{d^5\sigma}{dE_1 d\Omega_1 d\Omega_2} &\approx \frac{4\pi^2}{\omega c} k_1 k_2 |f(\mathbf{k}_1, \mathbf{k}_2, \hat{\boldsymbol{\epsilon}}; R_{eq})|^2 \int dR\, \chi_0(R)^2 \\
&= \frac{4\pi^2}{\omega c} k_1 k_2 |f(\mathbf{k}_1, \mathbf{k}_2, \hat{\boldsymbol{\epsilon}}; R_{eq})|^2.
\end{aligned}$$

(34)

Comparisons between fixed-nuclei calculations and measurements of quantities that probe only the vibrational ground state of a molecule are made using this approximation in many other contexts.

III. DISCRETIZATION OF THE DRIVEN SCHRÖDINGER EQUATION AND NUMERICAL METHODS FOR ITS SOLUTION

ECS is most easily implemented by using numerical grid methods or with basis functions that have compact support so that the derivative discontinuity at R_0 can be handled exactly. For the present study, we will present results using two independent implementations of ECS. These two separate computational efforts provide a powerful check on the consistency of the results obtained and allow us to better assess the convergence of the final results. In our earlier studies of DPI we used B-splines, which are easily adapted to handle ECS [32]. This allowed us to exploit a well-developed existing technology [33,34], which we had previously used in our studies of He double ionization [10,35] and in our initial studies of H_2 DPI [18]. We have since developed a second implementation that uses finite-element and DVR functions [36] in a single-center expansion of the problem. The FEM-DVR offers an independent check on the results, as we have said, and also has some distinct computational properties that should provide an efficient path to larger systems. The two methods are briefly summarized below.

A. *B*-splines

B-spline methods are well established as widely applicable tools for the evaluation of atomic and molecular continuum states [17,33,34]. Implementation of B-splines in the context of ECS was first proposed by McCurdy and Martín [32]. Details of the ECS and B-spline method can be found in the latter reference, so only a brief summary is given here. B-splines that scale according to the ECS transformation are simply defined by setting a series of knots $t_i \leq t_{i+1}$ on the

complex contour and by using the usual recursion relation [37] for B-splines of order k,

$$B_i^k(r) = \frac{r - t_i}{t_{i+k-1} - t_i} B_i^{k-1}(r) + \frac{t_{i+k} - r}{t_{i+k} - t_{i+1}} B_{i+1}^{k-1}(r) \quad (35)$$

together with the definition of B-splines of order $k=1$

$$B_i^1(r) = \begin{cases} 1, & \text{for } t_i \le r < t_{i+1} \\ 0, & \text{otherwise} \end{cases}. \quad (36)$$

Once the recursion is taken to third order ($k=3$) one has a set of the familiar (smooth) quadratic splines. Higher orders provide more spline functions in the basis covering successively larger numbers of knots as the order is increased (only k B-splines are different from zero at a given value of r). They also give more continuous derivatives as the order is increased. A basis of B-splines is defined by a grid of break-points, ξ_i, coinciding with the knots t_i (which may be multiple), that appear in the recursion relation above. In most applications, multiple knots are only used near the borders (e.g., at the origin to provide more flexibility in this region). Thus the number of knots is only slightly larger than the number of breakpoints. The breakpoints can be placed arbitrarily on this contour but one of them and its corresponding knot must be placed at $t_i = R_0$. In this way, B_i^k has a discontinuous first derivative with respect to r at $r = R_0$, because the derivative of the contour itself is discontinuous at that point. The discontinuity in the first derivative of all the B-splines that span the point R_0 is essential to reproduce that of the exact wave function. The middle panel of Fig. 1 shows a typical B-spline basis of order $k=8$ and the discontinuities of the first derivatives at $r = R_0$. Only B-splines that straddle the point R_0 have both real and imaginary components. All other B-splines are real, whether they are on the complex part of the contour or not.

With the above definitions, all one-electron matrix elements are reduced to sums of complex integrals between breakpoints. In each interval, the integrals are performed using a Gauss-Legendre quadrature. Only those integrals involving B-splines that are both different from zero in a given interval need to be evaluated. For the two-electron problem, we construct a product basis by combining B-spline functions for each radial electron coordinate with spherical harmonics for the angular variables. A "configuration" in the B-spline representation is thus given by

$$\Theta_{ijab}(\mathbf{r}_1, \mathbf{r}_2) = \mathcal{A}\left[\frac{B_i(r_1)}{r_1} Y_{l_a m_a}(\hat{\mathbf{r}}_1) \frac{B_j(r_2)}{r_2} Y_{l_b m_b}(\hat{\mathbf{r}}_2) \right]$$

$$\equiv \mathcal{A}[\Phi_{i,a}(\mathbf{r}_1) \Phi_{j,b}(\mathbf{r}_2)], \quad (37)$$

where $\mathcal{A}$ is, respectively, the symmetrization or antisymmetrization operator for singlet or triplet spin multiplicity. For simplicity in the notation, the order of the B-splines k has been omitted. It is straightforward to construct a representation of the Hamiltonian in this basis. The two-electron integrals, for example, are of the form

$$\left\langle \mathcal{A}[\Phi_{i,a}(\mathbf{r}_1)\Phi_{j,b}(\mathbf{r}_2)] \left| \frac{1}{|\mathbf{r}_1 - \mathbf{r}_2|} \right| \mathcal{A}[\Phi_{k,c}(\mathbf{r}_1)\Phi_{l,g}(\mathbf{r}_2)] \right\rangle$$

$$(38)$$

and are evaluated by making a multipole expansion of the interelectron repulsion. The angular portions of the two-electron matrix elements are evaluated analytically, while the radial portions are best handled by mapping the problem to an equivalent one involving the solution of Poisson's equation in an exterior complex-scaled B-spline basis. We refer the interested reader to Ref. [32] for details.

In these calculations we used an ECS radius of $R_0 = 40a_0$, and an ECS scaling angle of $\eta = 30°$. Tests of convergence of the calculations with respect to various computational parameters are presented below in Sec. IV. The combined B-splines and spherical harmonics representation converts Eq. (1) into coupled linear equations. Using angular momenta up to five leads to 22 coupled pairs of angular momenta for the two electrons in Σ_u symmetry. Using 60 eighth-order B-splines for each angular momentum then produces a Hamiltonian matrix of order $N = 79\,200$. Corresponding calculations in Π_u symmetry give 35 coupled pairs of angular momenta and the driven equation is of order $N = 126\,000$. The number of nonzero matrix elements is about 0.9% of the matrix.

B. Finite-element discrete-variable representation

The discrete-variable representation provides a numerical grid on which to perform the calculation, as well as an underlying expansion basis that allows the computed wave functions to be evaluated as a continuous function of the coordinates. The DVR was combined with the finite-element approach by Rescigno and McCurdy [36]. This extension allows for the treatment of exterior complex scaling by simply choosing the point R_0 to coincide with one of the finite-element boundaries.

Details of the FEM-DVR method can be found in Ref. [36] and in our recent review [19], so only a brief summary is given here. The DVR we use is built from a basis of normalized Lagrange interpolating polynomials defined on the interval $[a,b]$:

$$f_i(x) = w_i^{-1/2} \prod_{j \ne i} \frac{x - x_j}{x_i - x_j}. \quad (39)$$

These functions have the property that, when evaluated at the points $\{x_i\}$,

$$f_i(x_j) = \delta_{i,j}/\sqrt{w_i}. \quad (40)$$

The points $\{x_i\}$ and weights $\{w_i\}$ are in turn derived from a Gauss-Lobatto quadrature [38], which is similar to the more familiar Gauss-Legendre quadrature, except that two of the points are constrained to coincide with the interval endpoints. Under the Gauss quadrature rule, the functions are orthonormal and provide a diagonal representation of any local operator

$$\int_a^b f_i(x)V(x)f_j(x)dx \approx \sum_{k=1}^n f_i(x_k)V(x_k)f_j(x_k)w_k = V(x_i)\delta_{i,j}.$$

(41)

The kinetic energy operator is not diagonal in the DVR basis, but its matrix elements are given by simple analytic formulas [36]. Since Gauss-Lobatto quadrature explicitly includes the end points as quadrature points, it is possible to combine this particular variety of DVR with the finite-element method. We simply divide the ECS contour for the radial coordinate of each electron into one-dimensional finite elements with one of the boundaries coinciding with the point R_0 where the real and complex parts of the contour join.

For the full problem, we again construct (unsymmetrized) product basis functions Ω by combining DVR functions for each radial electron coordinate with spherical harmonics for the angular variables:

$$\Omega_{ijab}(\mathbf{r_1},\mathbf{r_2}) = \frac{f_i(r_1)}{r_1}Y_{l_am_a}(\hat{\mathbf{r_1}})\frac{f_j(r_2)}{r_2}Y_{l_bm_b}(\hat{\mathbf{r_2}}).$$

(42)

The one-electron nuclear attraction and two-electron repulsion integrals are again evaluated by making a multipole expansion of the operators and carrying out the angular parts of each integral analytically, reducing the problem to the evaluation of radial integrals. For example, the radial portion of the two-electron integrals that must be evaluated are of the form

$$\langle ij\|kl\rangle = \int_0^{r_{\max}}dr\int_0^{r_{\max}}dr'f_i(r)f_k(r)\frac{r_<^\ell}{r_>^{\ell+1}}f_j(r')f_l(r').$$

(43)

Gauss-Lobatto quadrature gives a poor approximation for the integrations in Eq. (43), because it effectively expands the derivative discontinuity in the potential $r_<^\ell/r_>^{\ell+1}$ in a basis of polynomials. However we can restore the validity of the underlying Gauss quadrature by replacing the integral with an equivalent Poisson differential equation which is solved using the DVR representation. Details can be found in [19]. The key result is that the DVR again gives a diagonal representation of the radial two-electron matrix elements

$$\langle ij\|kl\rangle \propto \delta_{i,k}\delta_{j,l}.$$

(44)

This property simplifies the evaluation of the Hamiltonian, which has a sparse structure in the DVR representation. For example, using 15th-order DVR with 6 finite elements gives 83 radial functions for each electron. With $l_{\max}=7$, there are 168 two-electron angular configurations and the size of the Hamiltonian matrix is $N=168\times83^2=1\,157\,352$. However, of the $N^2\approx1.3\times10^{12}$ Hamiltonian elements, only $\approx2.2\times10^8$ are nonzero. For this reason, we found it practical to carry out calculations in the FEM-DVR representation using an unsymmetrized basis and were able to systematically increase the number of angular terms until the results were converged. A final point to bear in mind is that, although the solution of the first-order equation in the FEM-DVR basis gives the wave function at discrete radial points, the underlying basis has a continuous representation given by Eq.

(39), which allows us to evaluate the wave function at any desired point. The continuous representation simplifies the computation of the surface integrals over the hypersphere needed in the evaluation of the ionization amplitudes.

C. Iterative methods of solution of the linear equations

After discretization of the radial degrees of freedom using the basis functions discussed in the previous section, Eq. (1) becomes a set of linear equations of the form $Ax=b$ in which the matrix A is sparse, complex symmetric, and indefinite. We use a Krylov subspace iterative method to find a solution. The approach is similar to the methods used to solve the electron impact ionization problem for hydrogen [39].

The convergence of iterative methods, in general, is determined by the location of the eigenvalues of A in the complex plane [40]. In our problem, the matrix A represents the complex-scaled Hamiltonian of a scattering problem and has most of its eigenvalues lying in the fourth quadrant of the complex plane. Many of these eigenvalues accumulate in a small region close to the origin, but there are also series of eigenvalues that start from the origin and spread out into the fourth quadrant. This distribution of eigenvalues of the matrix A leads to a large condition number (ratio of largest eigenvalue to the smallest eigenvalue) and the straightforward application of an iterative method to this problem leads to very slow convergence.

Instead of solving the matrix $Ax=b$, we choose to solve the matrix problem $M^{-1}Ax=M^{-1}b$ that has the same solution x. However, we construct a matrix M, such that the product $M^{-1}A$ has a spectrum that leads to fast convergence of the iterative methods. Rewriting the matrix problem like this is a well-known form of "preconditioning" and the mathematical properties of this procedure are well understood [41].

We derive a matrix M from A by reducing A to a block diagonal form through neglect of the coupling elements between the angular parts of the basis functions. The basis functions Θ_{ijab} (or Ω_{ijab}) have angular parts $Y_{l_am_a}(\hat{r}_1)Y_{l_bm_b}(\hat{r}_1)$, and when the two-electron Hamiltonian is discretized with these basis functions, the nuclear attraction and the electron-electron repulsion will introduce nonzero matrix elements between different basis functions with angular quantum numbers $l_am_al_bm_b$ and $l_{a'}m_{a'}l_{b'}m_{b'}$. The preconditioning matrix M is constructed by neglecting these angular couplings, but keeping the radial couplings between the basis functions within each $l_am_al_bm_b$ block of the matrix. Thus, the preconditioning matrix is

$$M_{ijab,i'j'a'b'} = \langle\Theta_{ijab}|H-E|\Theta_{i'j'a'b'}\rangle\delta_{l_al_{a'}}\delta_{l_bl_{b'}}\delta_{m_am_{a'}}\delta_{m_bm_{b'}}$$

$$= A_{ijab,i'j'a'b'}\delta_{l_al_{a'}}\delta_{l_bl_{b'}}\delta_{m_am_{a'}}\delta_{m_bm_{b'}}.$$

(45)

The matrix M has now a block diagonal structure with blocks that are n^2 by n^2, where n is the number of radial basis functions. The spectrum of the matrix M also has most of its eigenvalues in the fourth quadrant of the complex plane, similar to the full matrix A, but at slightly different locations.

It is, therefore, no surprise that the matrix $M^{-1}A$ has its eigenvalues clustered around one with a ratio of the largest to
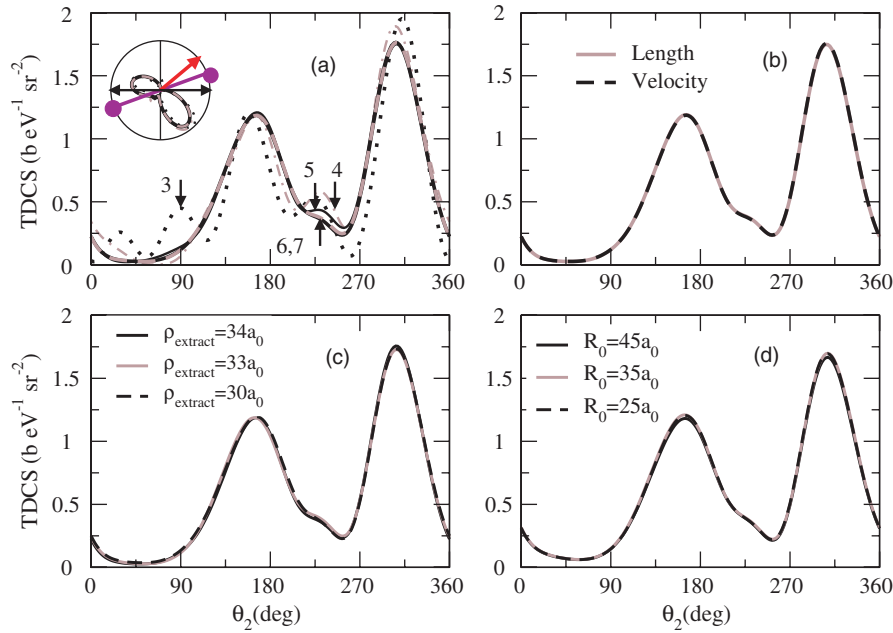
FIG. 3. (Color online) Convergence of calculated TDCS. In this example, the molecule, ejected electrons, and polarization vector are coplanar, and the TDCS, plotted as function of one ejection angle θ_2. The angle between molecule and polarization axis is $\theta_{mol}=20°$ and the angle between fixed electrons (with 80% of available energy) and polarization axis is $\theta_1=40°$. (a) Convergence of the velocity representation as a function of partial-wave angular momentum l_{max}. Numbers labeling curves refer to the maximum value of l included. (b) Length- and velocity-gauge results for TDCS from DVR calculations with $l_{max}=7$. (c) Convergence with hyper-radius at which amplitude is extracted. ECS radius R_0 is fixed at $35a_0$ while the amplitude is computed at three different values of hyper-radius. (d) Convergence with increasing R_0. Hyperradius ρ at which the amplitude is calculated is fixed at $24a_0$, while the value of R_0 is varied.

the smallest eigenvalue of approximately two. Such a problem is easily solved with a Krylov subspace method. We find the solution using the generalized minimum residual method to machine precision within 50 iterations in the case of the *B*-spline calculations, and within 20 interactions when using the FEM-DVR basis. Each step of the preconditioned Krylov iteration requires the solution of the matrix problem $Mx'=v$. This problem, however, is much less demanding to solve than the original problem, since the blocks of M are not coupled. It is solved block by block with a direct solver.

IV. CONVERGENCE TESTS

All of the calculations reported here were carried out at the equilibrium internuclear distance $R_{eq}=1.40$ bohrs. We begin by examining the convergence with respect to the number of angular momenta included in the expansions of both the H_2^+ wave function in Eq. (18) and the outgoing wave function $\Psi_{sc}^{+(M)}$ in Eq. (19). The same maximum value of l was used in both expansions. For this test we choose an example geometry for which the TDCS is small and involves roughly equal contributions from the Σ_u ($M=0$) and Π_u ($M=\pm1$) components of the wave function. Figure 3(a) shows that the velocity gauge results using the FEM-DVR radial basis are converged except for very minor details when angular momenta up to $l=5$ have been included and that by $l=6$ the calculations are converged to graphical accuracy even for the small TDCS values.

A comparison of results in the length and velocity gauges in calculations including up to $l=7$ using the FEM-DVR ra-

dial basis is presented in Fig. 3(b), and shows that the two gauges produce graphically indistinguishable cross sections. This comparison is typical of the TDCS for other geometries of molecular orientation and outgoing electrons as well, and it is a test of the completeness of both the angular and radial basis being used. It is also, of course, a test of the quality of the initial state wave function. In earlier calculations [18], we tested the variation of the TDCS by increasing the maximum angular momentum included in the initial state from $l=6$ to $l=8$, and found no changes. We conclude that calculations using up to $l=7$ in both initial and final states are effectively converged with respect to angular momentum contributions.

It is instructive, when discussing convergence with respect to angular momentum, to contrast the behavior of low and high partial-wave radial components of the full scattered wave. Figure 4 shows two such components for the case of a fully converged calculation in Σ_u symmetry. The interesting thing to note, apart from the relative magnitudes of the two components, is the fact that, while the single ionization contributions to the wave function are clearly visible in the low partial-wave component along the left edge of the figure, the high partial-wave component contributes only to double ionization. This is a striking indication of the fact that DPI probes parts of the wave function that reveal the effects of electron correlation.

The surface integral in Eq. (22) encloses a finite volume of hyper-radius ρ_0, and a key question about the convergence of these calculations is whether that finite volume is large enough to allow accurate extraction of the physical amplitude for double ionization. We test the dependence of the
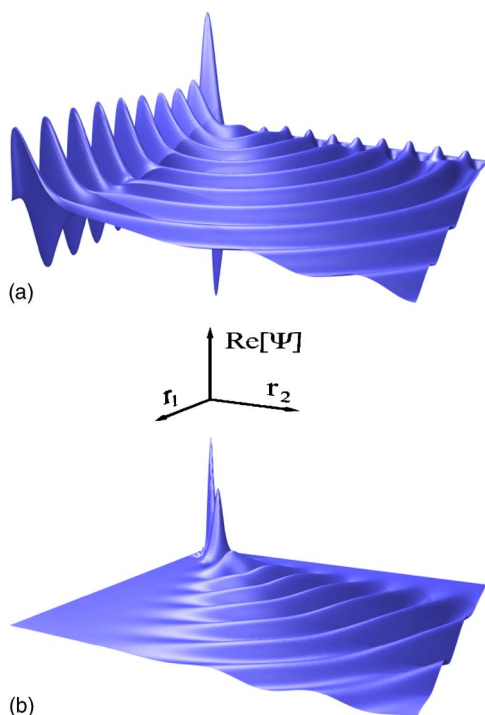
FIG. 4. (Color online) Real part of partial-wave components of direct part of the full scattered wave function $\Psi_{sc}^{+(0)}$ for $(l_1,m_1,l_2,m_2)=(2,0,1,0)$ (a) and $(4,-4,7,4)$ (b). The magnitude of the wave function scale is given by the length of the z axis with magnitude $1.0\times10^{-2}a_0^{-1}$ (a), $1.0\times10^{-5}a_0^{-1}$ (b). The ranges of r_1 and r_2 are zero to 35.0 bohrs.

calculated TDCS on ρ_0 in Fig. 3(c), where we find no visible changes in the computed double ionization cross section once ρ_0 is greater than about $30a_0$.

Finally, we comment on the results of varying the ECS parameters R_0 and η. We show in Fig. 3(d) that varying R_0 from $25a_0$ to $45a_0$ again leaves the TDCS unchanged to graphical accuracy. Convergence with respect to R_0 is another test of the effective completeness of the radial basis. The variation of η from $25°$ to $40°$ produces even smaller changes in the TDCS, and this stability is a consequence of the fact that both the B-spline and FEM-DVR bases treat the derivative discontinuity of the ECS wave function at R_0 exactly [19].

Comparing the FEM-DVR and B-spline results in the velocity gauge using angular momenta up to $l=5$ in Fig. 5 shows only very small differences of the order of a few percent. This comparison verifies that the initial results for the TDCS from B-spline calculations presented in Ref. [18] were converged. The fact that most of the numerical details of those two calculations are different lends additional confidence to the calculations we present here. We note, however, that several of the TDCS plots in Ref. [18] were mislabeled with respect to the orientation of the molecule, and that the correct labeling of those results is discussed below.

Unless otherwise specified, the calculations presented below were performed using the FEM-DVR basis in the velocity gauge with the parameters described in Sec. III B, and make use of angular momenta up to $l=7$ and $R_0=35a_0$.
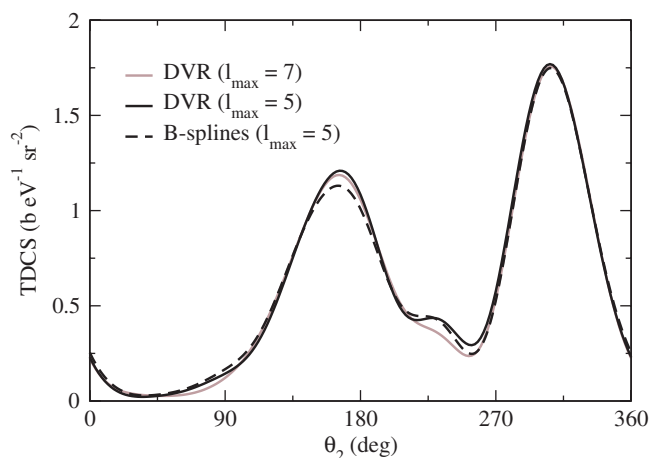
FIG. 5. (Color online) Comparison of TDCS computed using DVR and B-splines. The geometry is the same as in Fig. 3. Shown are results for a B-spline and DVR calculation using $l_{max}=5$, and also a DVR calculation using $l_{max}=7$.

V. THE COMPUTED CROSS SECTIONS FOR DOUBLE PHOTOIONIZATION OF H_2

The SDCS for double ionization by a 75 eV photon, computed at the equilibrium internuclear distance of H_2 is shown in the upper panel of Fig. 6, and corresponds to an integrated cross section of 2.61 kb. Two features of the SDCS at this energy are immediately apparent. First, it is relatively flat in shape, as can be expected for both atomic and molecular double photoionization at these energies. Second, the contribution to Eq. (26) of the final continuum of Π_u symmetry is approximately 13.5 times larger than that of Σ_u symmetry at equal energy sharing. That means that the perpendicular component, $d\sigma^{(\Pi)}/dE_1$, in Eq. (26) is about 6.75 times larger than that of the parallel component, $d\sigma^{(\Sigma)}/dE_1$, at that energy sharing. The corresponding β parameter, defined as

$$\beta = \frac{2\left(\dfrac{d\sigma^{(\Sigma)}}{dE_1} - \dfrac{d\sigma^{(\Pi)}}{dE_1}\right)}{\left(\dfrac{d\sigma^{(\Sigma)}}{dE_1} + 2\dfrac{d\sigma^{(\Pi)}}{dE_1}\right)}, \tag{46}$$

is plotted in the lower panel of Fig. 6. Its value at equal energy sharing is -0.788 and varies by less than 1.5% over the entire range of energy sharings. Our result is in good agreement with the measured value of Gisselbrecht *et al.* [4] who report $\beta\approx-0.75\pm0.1$, while the earlier measurements of Kossmann *et al.* [42] gave $\approx-0.68\pm0.04$. The difference in the magnitudes of the perpendicular and parallel contributions to the double photoionization cross section is a fundamental difference between the case of H_2 and the isoelectronic atomic case of helium. As we will see below, interference in the TDCS between the Σ_u and Π_u amplitudes for various molecular geometries is an important cause of the differences between the atomic and molecular cases.

In Figs. 7–9 we show the TDCS for in-plane geometries in which one electron is fixed in a direction perpendicular to the polarization vector, while the molecule is rotated in the same plane through $90°$. The three figures show the cases in
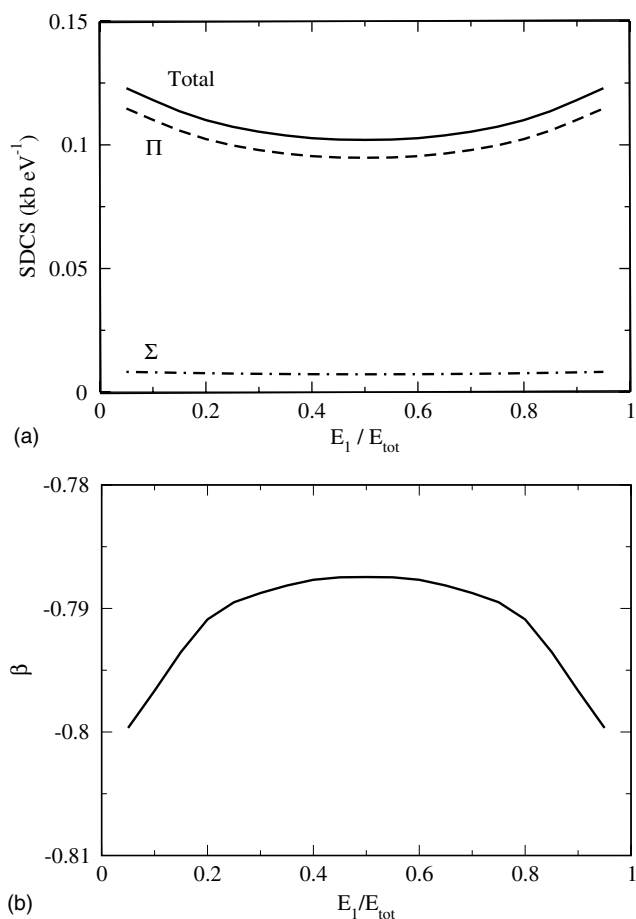
FIG. 6. Upper panel: SDCS for photon energy of 75 eV computed at equilibrium internuclear distance, showing Π_u and Σ_u contributions of Eq. (26). Integral cross section is the integral of this SDCS from 0 to E_{tot}. Lower panel: β parameter for the same photon energy and internuclear distance.

which the fixed electron carries away 20%, 50%, and 80% of the available energy, respectively. In the case of helium there would be a single TDCS corresponding to each six panel figure for H_2. We see a strong molecular effect in each case as the molecule is rotated with respect to the polarization vector. Indeed, these figures show the effect of nuclear attraction on the slower outgoing electron for a set of cases for which no simple symmetry selection rules apply. Attraction to the nuclei tends to orient some parts of the ejection pattern along that axis, but this effect is strongly modified by the forces of electron repulsion and the applied radiation field.

In the atomic case, for equal energy sharing, the TDCS consists of two lobes with an exact zero where the two electrons both depart perpendicular to the polarization vector. Except in the molecular geometries where one lobe is so small as to be almost invisible, the TDCS for H_2 shows a two lobed structure reminiscent of the atomic cross section, but strongly perturbed by the lower molecular symmetry. The difference in the sizes of the parallel and perpendicular components of the cross sections is explicitly demonstrated by the magnitudes of the TDCS in the top left and bottom right panels of each figure, and those two contributions interfere coherently to produce the TDCS at all but the 0° and 90° geometries.
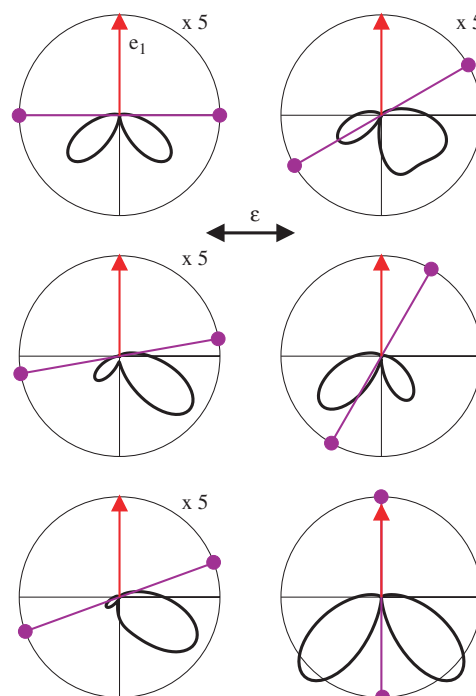
FIG. 7. (Color online) TDCS for in-plane geometries with unequal energy sharing. Fixed electron (single ended arrows) at 90° from the polarization with 20% of available energy. Left column top to bottom: $\theta_{mol}=0°$, 10°, and 20°. Right column top to bottom: $\theta_{mol}=30°$, 60°, and 90°.

Out-of-plane cases show the interference between the parallel and perpendicular components more clearly. In Figs. 10–12, we show a similar sequence of TDCS plots, this time with the fixed electron coming out of the plane towards the viewer. The three figures again show 20%, 50%, and 80% of the available energy, respectively. In all three figures we see the striking effect that the principal axis of the TDCS, which is parallel to the polarization vector when the molecule and the polarization are aligned, appears to rotate by 180° when the molecule is rotated by only 90°.

The reason for this apparent behavior is that as the molecule is rotated away from the parallel configuration, the Π_u component, whose contribution to the TDCS is largely perpendicular to the molecule, grows rapidly from zero as the angle increases. When the molecule reaches 30° (top right panel in Figs. 10–12) the Π component already dominates and continues to rotate with the molecule as the angle is increased.

Comparing the out-of-plane to in-plane geometries we also note a considerably smaller difference between the magnitudes of the purely parallel and purely perpendicular geometries in which the molecule makes an angle of 0° and 90° to the polarization, respectively.

A multitude of shapes in the TDCS is revealed when the fixed electron and molecular axis are chosen at different angles. Viewing them in three dimensions gives the best general impression of the qualitative features of the TDCS. For example, the out-of-plane cases in Figs. 10–12 are given a new perspective by Fig. 13 which shows an out-of-plane case with the molecule at 15° from the polarization vector
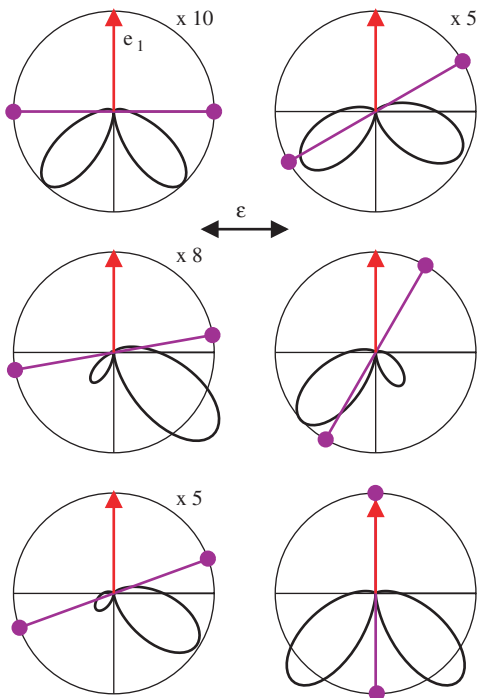
FIG. 8. (Color online) Same as in Fig. 7, except the fixed electron has 50% of the available energy.

and reveals that they are each slices through the face of a three-dimensional TDCS that is much larger behind the plane in which they are plotted.

To give a sense of the variety of the three-dimensional shapes of the TDCS that are characteristic of molecular double photoionization in this case we plot the TDCS for
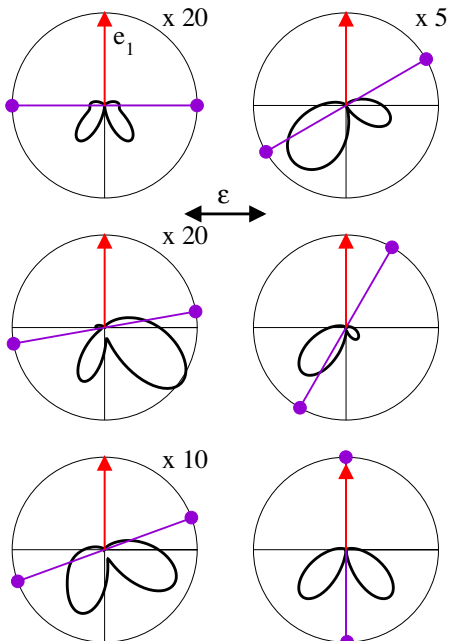

FIG. 9. (Color online) Same as in Fig. 7, except that the fixed electron has 80% of the available energy.
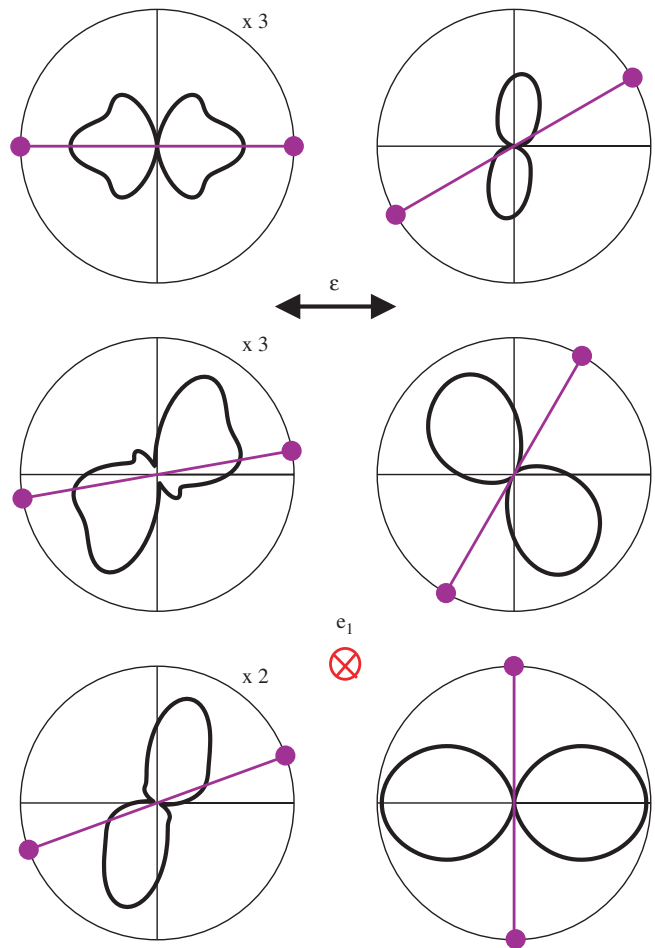
FIG. 10. (Color online) TDCS for out-of-plane geometries with unequal energy sharing. Fixed electron perpendicular to the page with 20% of available energy. Left column top to bottom: θ_{mol} =0°, 10°, and 20°. Right column top to bottom: θ_{mol}=30°, 60°, and 90°.

another geometry in Fig. 14. In this case the molecule and fixed electron are both 20° from the polarization direction. In contrast to the two lobes that would appear in the angular distribution for atomic helium, the strong interference between the Σ and Π contributions produces a three lobed TDCS that cannot be explained by any simple model. We should note that this figure was plotted incorrectly in Ref. [18] and that a figure similar to Fig. 13 was presented with the molecule drawn at 15° on the opposite (wrong) side of the polarization, but that all the other figures in that preliminary report were correct.

VI. COMPARISON WITH EXPERIMENTAL MEASUREMENTS

A. Experimental resolutions

The momentum imaging experiments on this system [1–4] all involve finite ranges of acceptance for the angles of the fixed electron, plotted electron, and molecule. The TDCS plots of Sec. V demonstrate that the cross section can change rapidly with those angles, and so to make meaningful com-
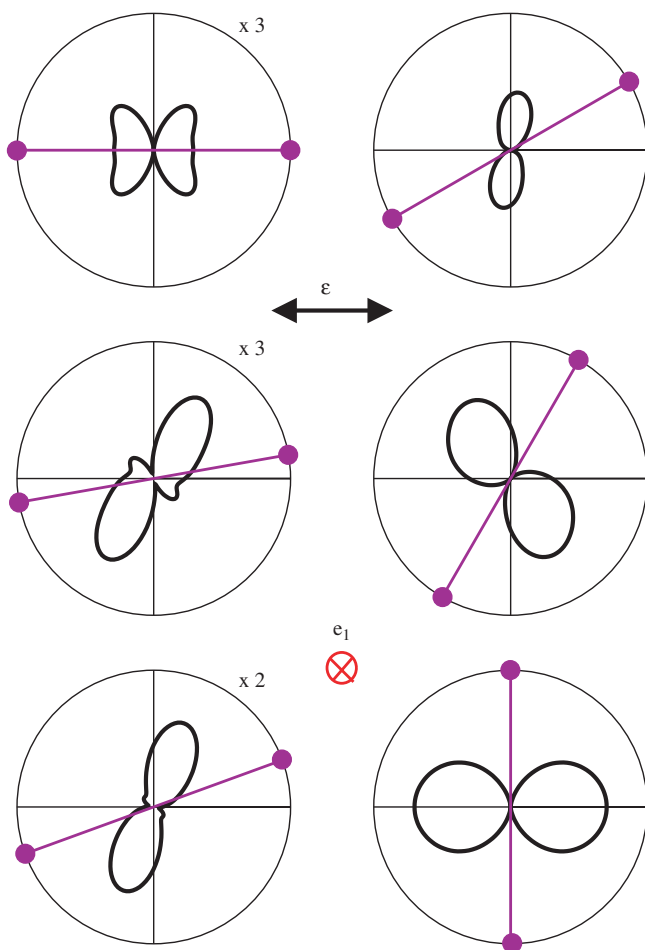
FIG. 11. (Color online) Same as in Fig. 10, except that the fixed electron has 50% of the available energy.

FIG. 12. (Color online) Same as in Fig. 10, except that the fixed electron has 80% of the available energy.

parisons with experiment we must integrate the calculated cross sections over the acceptance angles. Moreover, the experimental measurements are reported with finite resolution for the energy sharing between the two electrons, and we must also integrate over that range of energy sharings in comparisons between theory and experiment. In all the cases we report here the resolution for energy sharing was ±10%. However, the conventions for expressing angular resolutions differ in the two current sets of experiments.

For the experiments of Weber and co-workers [1–3] a plane is defined by the fixed electron (or the molecular axis in the case of Fig. 21) and the direction of polarization. Angle ranges refer to in-plane and out-of-plane angles with the analogy to a globe with the plane at the equator. In-plane angles refer to rotation in the plane (longitude) with all angles equally weighted. The out-of-plane angles are weighted by a factor of $\sin(\phi)$. For out-of-plane cases, the acceptance range of the molecule in Fig. 17, or the fixed electron in Fig. 21, is a conical range given by all points on the sphere within a fixed angle of the perpendicular to the plane. Typical acceptance ranges for these experiments range from ±12° for the electrons to ±45° for the molecule. The exact values are given in Ref. [3] as cited in each figure below. Since the experimental results of Weber *et al.* are reported in arbitrary units but are internormalized within
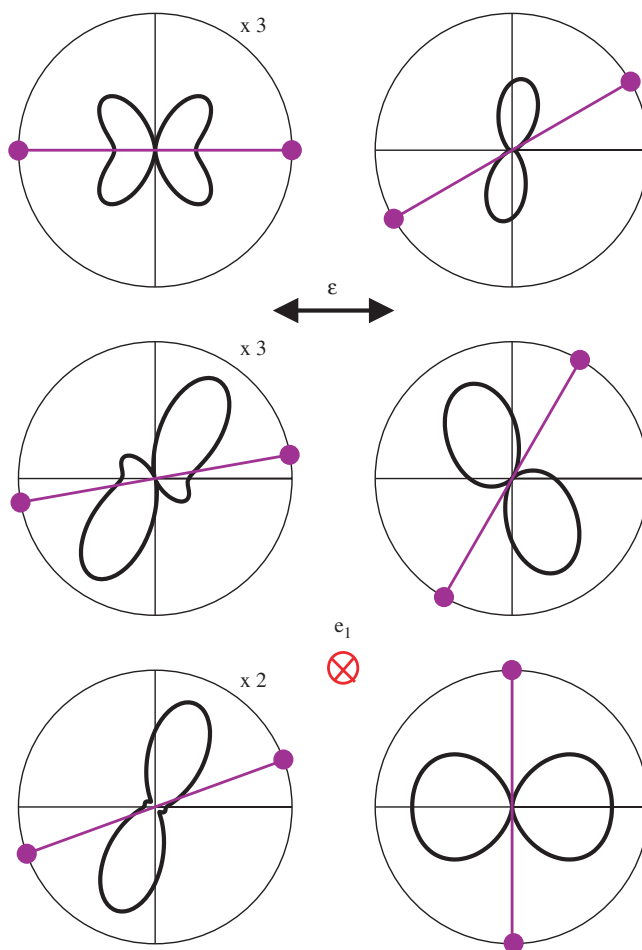
each panel set, we have chosen, in each figure, a scaling factor that gives the best overall fit to our averaged data.

For the experiments of Gisselbrecht *et al.* [4], the averaging was done over spherical polar angles defined with the polarization direction as the *z* axis and a plane defining the zero of the azimuthal angles. In the coplanar case of Fig. 18, this plane is defined by the polarization and the fixed electron directions. In Fig. 19 the plane is now defined by the polarization and the plotted electron since the fixed electron is parallel to the polarization direction. In Fig. 20, the plane is defined to be the one perpendicular to the plane containing the polarization vector and the fixed electron, but containing the polarization vector. In all cases averaging over the acceptance angles was performed for each quantity (electron or molecule) according to

$$\sigma_{\text{ave}} = \frac{\int_{\phi_1}^{\phi_2}\int_{\theta_1}^{\theta_2}\sigma(\theta,\phi)\sin(\theta)d\theta\,d\phi}{\int_{\phi_1}^{\phi_2}\int_{\theta_1}^{\theta_2}\sin(\theta)d\theta\,d\phi}. \tag{47}$$

For these experiments the exact ranges of acceptance are given in Ref. [4], and typically are about ±20° for the electrons and ±20° to ±45° for the molecule. The results of
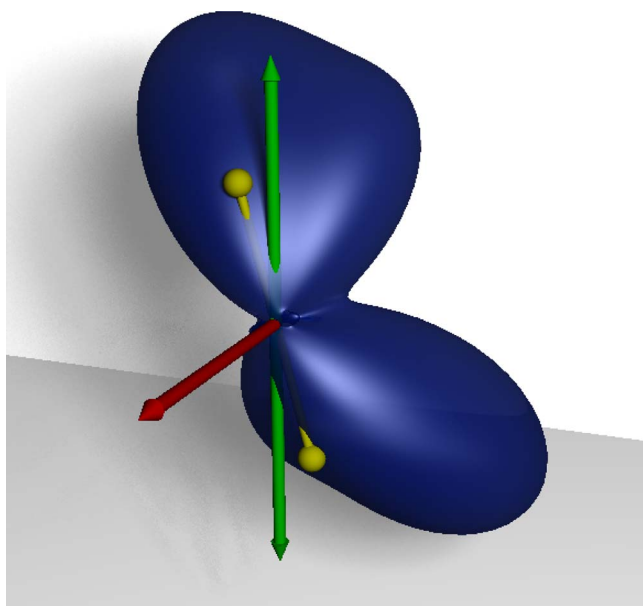
FIG. 13. (Color online) 3D plot of TDCS for a case of equal energy sharing with fixed electron (red arrow) perpendicular to polarization axis (green) with molecule making an angle of 15° with the polarization axis. Results shown were obtained from *B*-spline calculations. Note that the molecular orientation was plotted incorrectly in Ref. [18].

Gisselbrecht *et al.* were reported in absolute units, but their cross sections are differential in both E_1 and E_2 and, therefore, effectively differential in KER. Since our cross sections were computed for a single internuclear distance, we chose a single scaling factor in all cases for comparing our averaged results with their experiments in Figs. 18–20.
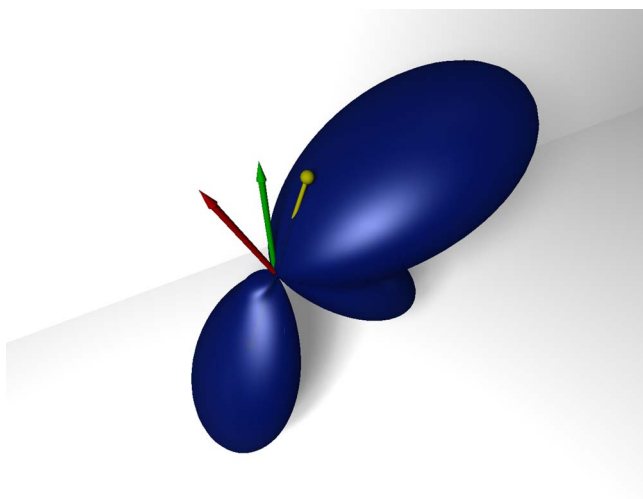
FIG. 14. (Color online) 3D plot of TDCS with molecule (yellow) and fixed electron (red) at 20° from polarization vector (green) and with fixed electron having 10% of the available energy. Results shown were obtained from *B*-spline calculations. Note that this case was plotted incorrectly in Ref. [18].
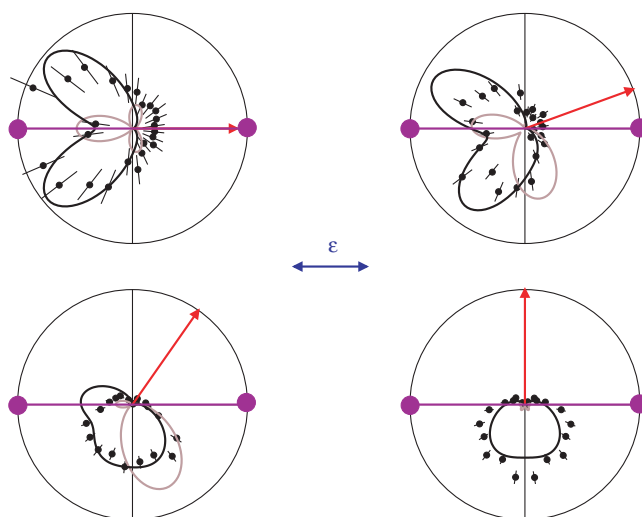

FIG. 15. (Color online) Comparison with experiments of Weber (Fig. 5.69 of Ref. [3]). The molecular axis is parallel to the polarization direction (horizontal). The fixed electron (arrow), with 90% of the available energy is at (left to right in each row) 0°, 20°, 55°, and 90° to the polarization direction. Current results are shown unaveraged (light solid curves) and averaged over experimental acceptance angles (black solid curves).

B. Comparison with measured cross sections

We begin by comparing the calculated TDCS for some in-plane cases, both as calculated for the central geometry and energy sharing, and also averaged over the experimental resolutions as described above, with the measurements of the relative cross sections of Weber [3] and absolute measurements of [4].

Figure 15 shows an unequal energy sharing case which, were it not for the finite acceptance angles, would be a case with only Σ_u contributions. However, averaging over acceptance angles incorporates a large contribution of the Π_u component which interferes with the Σ_u component to change both the magnitude and shape of the TDCS radically. The resulting agreement with the four internormalized measurements shown in Fig. 15 is dramatically improved, revealing how the finite resolution of the experiment obscures completely the Σ_u contribution to the angular dependence of the double photoionization process.

Figures 16 and 17 show two cases of experiments in the geometry that would have only Π_u contributions, but that are also modified by averaging over acceptance angles and energy resolution. Both figures are for unequal energy sharing with the fixed electron having 90% of the available energy. Here the changes in magnitude upon averaging over the experimental resolution are not as great as in Fig. 15 because the Π_u contribution dominates at most geometries. The changes in shape are also more modest, but the averaged results agree quite well with the experimental measurements except for some details. Note that while the panels of each of these figures are internormalized, the error bars are quite different in each case.

We can detect an interesting molecular effect by comparing the upper left panels of Figs. 16 and 17, where the po-
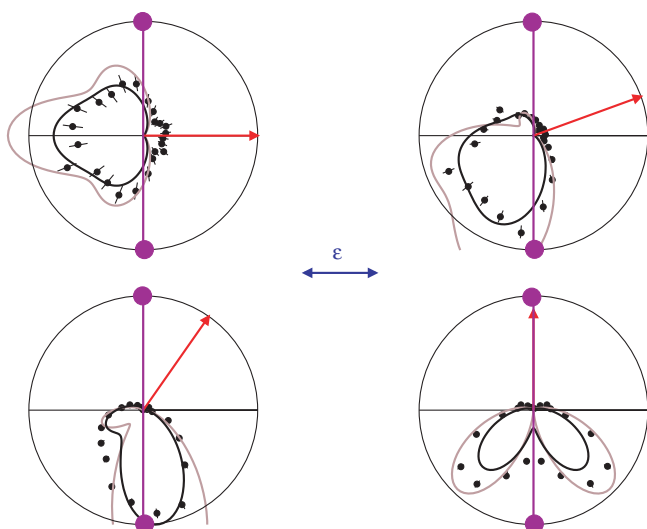
FIG. 16. (Color online) Comparison with experiments of Weber (Fig. 5.71 of Ref. [3]). The molecular axis is perpendicular to the polarization direction (horizontal). The fixed electron, (arrow) with 90% of the available energy is at (left to right in each row) 0°, 20°, 55°, and 90° to the polarization direction. Current results are shown unaveraged (light solid curves) and averaged over experimental acceptance angles (black solid curves).

larization direction and the fixed electron form a common axis about which there would be cylindrical symmetry in the case of helium. In the molecular case, however, the cylindrical geometry of the atomic case becomes flattened along the direction of the molecular axis (Fig. 16). While the effect is most clearly seen when comparing the unaveraged results, it is also evident in the averaged results, as well as in the experimental measurements.
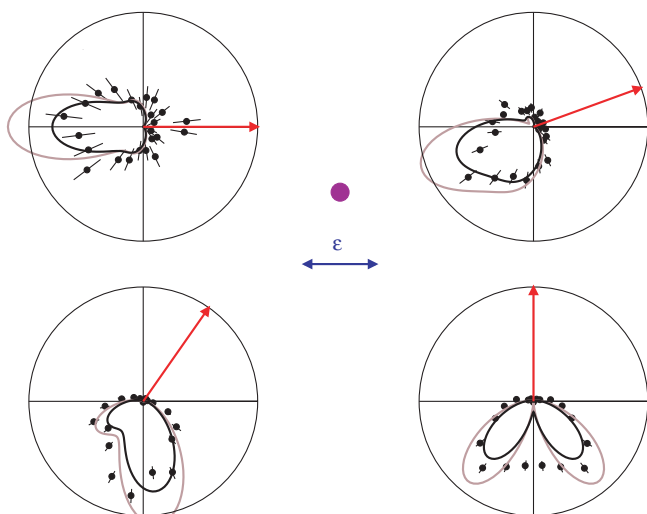

FIG. 17. (Color online) Comparison with experiments of Weber (Fig. 5.73 of Ref. [3]). The molecular axis is perpendicular to the polarization direction (horizontal) and perpendicular to the plane of the page. The fixed electron (arrow), with 90% of the available energy is at (left to right in each row) 0°, 20°, 55°, and 90° to the polarization direction. Current results are shown unaveraged (light solid curves) and averaged over experimental acceptance angles (black solid curves).
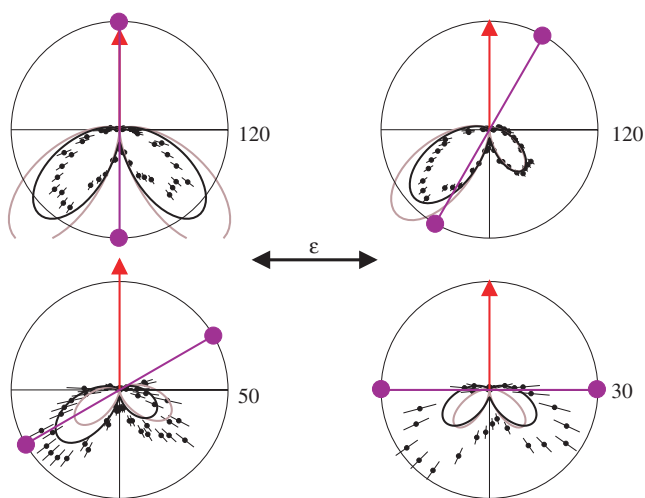

FIG. 18. (Color online) Comparison of averaged (black solid curves) and unaveraged (light solid curves) theoretical results with experimental data from [4] (points) for in-plane geometries with fixed electron (arrow) perpendicular to polarization and equal energy sharing. Molecule is at (top to bottom in each column) 90°, 30°, 60°, and 0° from polarization direction. The acceptance angles are those from Fig. 1 of the reference. Radii of the circles, marked to the right, give the magnitude of the cross section in units of (millibarns eV^{-2} sr^{-3}) as given in Ref. [4].

Turning to the recent experiments of Gisselbrecht *et al.* [4], Fig. 18 shows a comparison of the averaged and unaveraged calculated TDCS for an in-plane case with equal energy sharing. These measurements are absolute and have somewhat better statistics than those of Refs. [1–3]. In this figure the fixed electron is perpendicular to the polarization direction, while the molecule is rotated from perpendicular to parallel to the polarization. One sees how the averaged theoretical results agree both quantitatively and qualitatively with all but the smallest TDCS shown here.

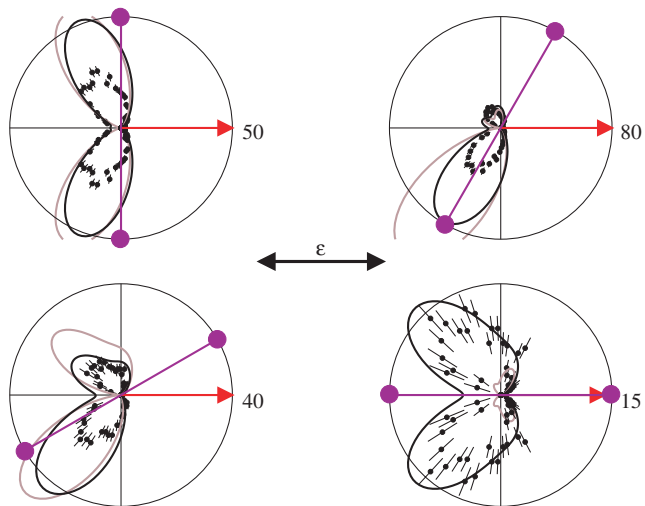In Fig. 19 we show another comparison with the measure-

FIG. 19. (Color online) As is Fig. 18, with fixed electron (arrow) parallel to polarization. The acceptance angles are those from Fig. 2 of the reference.
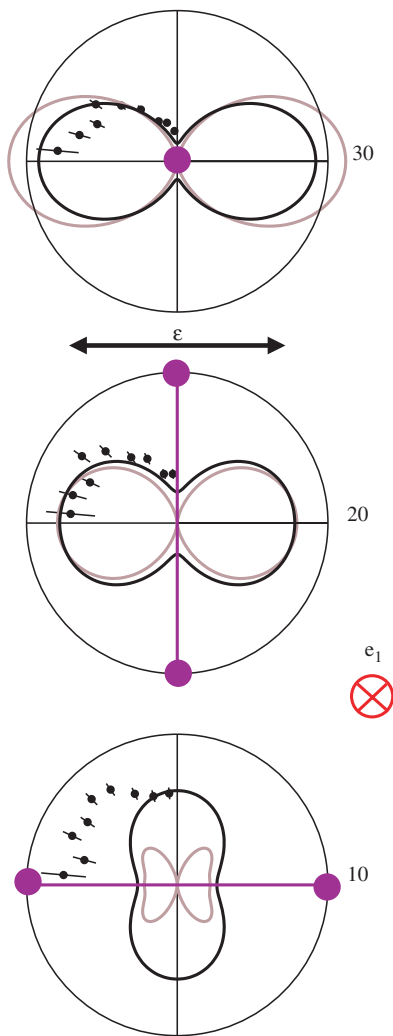
FIG. 20. (Color online) As is Fig. 18, for out-of-plane geometries. The acceptance angles are those from Fig. 3 of the reference.
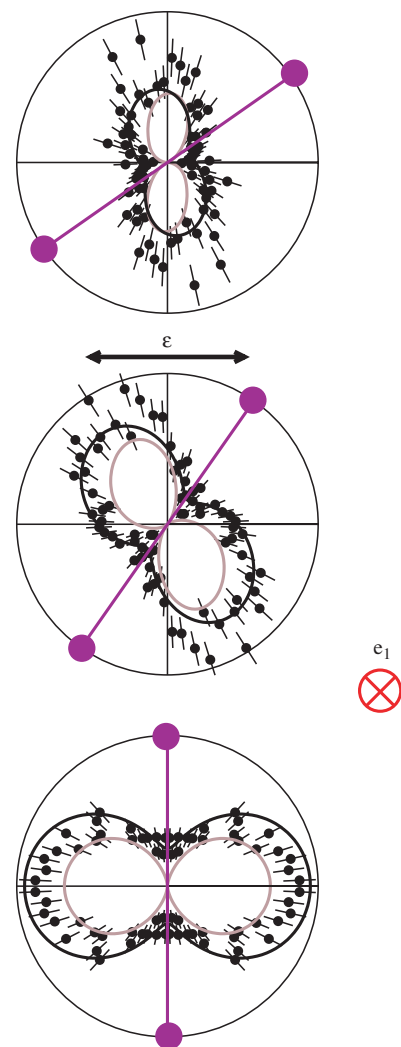

FIG. 21. (Color online) Comparison with experiments of Weber *et al.* [1], as recently corrected by Weber [43]. The fixed electron, with 50% of the available energy, is perpendicular, coming out of the page, while the molecule is oriented in the plane at (top to bottom) 35°, 55°, and 90° to the polarization direction (horizontal). Theoretical results are shown unaveraged (light solid curves) and averaged over experimental acceptance angles (black solid curves).

ments of [4], this time in an in-plane geometry with the fixed electron being ejected parallel to the direction of polarization. In this case the averaging is necessary to reproduce the correct shape, especially in the case where the molecule is ostensibly parallel to the polarization direction, but the quantitative agreement is poorer than that of Fig. 18. We note, however, that if we were to divide our results in Fig. 19 by a factor of 2, then the agreement with experiment would be very good. We have not done so, however, since the measurements of [4] were reported as absolute.

A comparison with out-of-plane measurements from the same experiment with one electron ejected towards the observer, and with the molecule either parallel or perpendicular to the direction of polarization is shown in Fig. 20. In this case averaging over acceptance angles is again most important for the geometry that samples angles in geometries where the molecule is near parallel to the direction of polarization. However, in that geometry the agreement with experiment is poorest.

A similar out-of-plane case from the experiments of Weber *et al.* [1,3] is shown in Fig. 21, this time with the molecule oriented at angles of 35°, 55°, and 90°. This is a

case close to that explored in Fig. 11 showing the apparent rotation of the cross section by 180° while the molecule rotates by 90°. A sign error in the presentation of the polar plots of the experiments originally reported [1,3] was recently discovered and corrected by Weber [43]. In this case the theoretical cross sections, averaged over the acceptance angles of the experiment, are in excellent agreement with the corrected experimental data, which beautifully display how the cross section rotates with the molecule.

VII. CONCLUSIONS

We have demonstrated the convergence of fixed-nuclei calculations of the cross sections for double photoionization of H_2 by a 75 eV photon, and provided a consistency check between two different numerical approaches to these calcu-

lations. Clear molecular effects are visible in the calculated TDCS and a range of sensitively varying shapes for these cross sections emerge when different geometries of photo-ejection are explored. Some of those shapes result from the interference of the parallel and perpendicular components of the double ionization amplitude, which have substantially different magnitudes.

The comparison with two sets of experiments reveal the necessity of averaging these calculations over experimental angular and energy resolutions. While agreement is generally acceptable, some discrepancies between experiment and theory for the TDCS remain. We also find that the angular resolutions inherent in the current generation of experiments obscure details of the TDCS that are clear signatures of molecular effects in the double photoionization process. Further work will be required to resolve the remaining discrepancies between converged theory and experiment and to verify the effects that are currently beyond experimental resolution.

In a subsequent presentation we will explore the variation of these cross sections with internuclear distance, first observed by Weber *et al.* [2]. Measurements have been performed for various ranges of kinetic energy release into the nuclear motion that map onto particular ranges of internuclear distance sampled by the ground state vibrational wave function. This intrinsically molecular effect and the degree to which it is sensitive to molecular electronic correlation will be targets of those calculations. In that study we will explore the consequences of accurately performing the integral of the amplitude over internuclear distance in Eq. (31) in lieu of making use of the delta function approximation to that integral.

ACKNOWLEDGMENTS

APPENDIX: RELATION BETWEEN DIRECT AND EXCHANGE AMPLITUDES

For the calculations using *B*-splines, an explicitly anti-symmetrized wave function was used, as expressed in Eq. (19). The resulting direct amplitude $F^{\text{dir}}_{l_1,l_2,j_1,\mu_1,j_2,\mu_2}(k_1,k_2)$ is defined in (22), and the corresponding exchange integral is defined as

$$
\begin{aligned}
&F^{\text{exch}}_{l_1,l_2,j_1,\mu_1,j_2,\mu_2}(k_1,k_2) \\
&= \frac{\rho_0}{2}\int_0^{\pi/2} d\alpha \left(\frac{\phi^{(c)}_{l_1,k_1}(r_1)}{k_1}\delta_{l_1,j_2} + R^{l_1\mu_2}_{j_2}(r_1) \right) \\
&\quad \times \left(\frac{\phi^{(c)}_{l_2,k_2}(r_2)}{k_2}\delta_{l_2,j_1} + R^{l_2\mu_1}_{j_1}(r_2) \right) \\
&\quad \times \left[\frac{\overleftarrow{\partial}}{\partial\rho} - \frac{\overrightarrow{\partial}}{\partial\rho} \right]_{\rho=\rho_0} \psi^{\text{exch}}_{j_1\mu_1,j_2\mu_2}(r_1,r_2).
\end{aligned}
\tag{A1}
$$

In practice it is unnecessary to calculate this integral separately, because we can make use of symmetry properties to relate this exchange amplitude to a direct amplitude.

If we replace $\psi^{\text{exch}}_{j_1\mu_1,j_2\mu_2}(r_1,r_2)$ with $\psi^{\text{dir}}_{j_1\mu_1,j_2\mu_2}(r_2,r_1)$ and then relabel the electronic coordinates by exchanging r_1 and r_2, we find

$$
\begin{aligned}
&F^{\text{exch}}_{l_1,l_2,j_1,\mu_1,j_2,\mu_2}(k_1,k_2) \\
&= \frac{\rho_0}{2}\int_0^{\pi/2} d\alpha \left(\frac{\phi^{(c)}_{l_1,k_1}(r_2)}{k_1}\delta_{l_1,j_2} + R^{l_1\mu_2}_{j_2}(r_2) \right) \\
&\quad \times \left(\frac{\phi^{(c)}_{l_2,k_2}(r_1)}{k_2}\delta_{l_2,j_1} + R^{l_2\mu_1}_{j_1}(r_1) \right) \\
&\quad \times \left[\frac{\overleftarrow{\partial}}{\partial\rho} - \frac{\overrightarrow{\partial}}{\partial\rho} \right]_{\rho=\rho_0} \psi^{\text{dir}}_{j_1\mu_1,j_2\mu_2}(r_1,r_2),
\end{aligned}
\tag{A2}
$$

which is equal to $F^{\text{dir}}_{l_2,l_1,j_1,\mu_1,j_2,\mu_2}(k_2,k_1)$. So we have a relationship between particular direct and exchange amplitudes,

$$
F^{\text{exch}}_{l_1,l_2,j_1,\mu_1,j_2,\mu_2}(k_1,k_2) = F^{\text{dir}}_{l_2,l_1,j_1,\mu_1,j_2,\mu_2}(k_2,k_1).
\tag{A3}
$$

Similar relations can be found for the reduced amplitudes $\mathcal{F}^{\text{dir,exch}(M)}_{l_1,l_2,\mu_1,\mu_2}(k_1,k_2)$.

[1] T. Weber *et al.*, Nature (London) **431**, 437 (2004).

[2] Th. Weber *et al.*, Phys. Rev. Lett. **92**, 163001 (2004).

[3] T. Weber, Ph.D. thesis, Institut fuer Kernphysik, Frankfurt, 2003 (unpublished), available at http://hsb.uni-frankfurt.de/web/publications/diplom_doktor/

[4] M. Gisselbrecht, M. Lavollee, A. Huetz, P. Bolognesi, L. Avoldi, D. P. Seccombe, and T. J. Reddish, Phys. Rev. Lett. **96**, 153002 (2006).

[5] J. Colgan, M. S. Pindzola, and F. Robicheaux, J. Phys. B **34**, L457 (2001).

[6] P. Selles, L. Malegat, and A. K. Kazansky, Phys. Rev. A **65**, 032711 (2002).

[7] A. S. Kheifets and I. Bray, Phys. Rev. A **65**, 022708 (2002).

[8] L. Malegat, P. Selles, and A. Huetz, J. Phys. B **30**, 251 (1997).

[9] A. Huetz, P. Selles, D. Waymel, and J. Mazeau, J. Phys. B **24**, 1917 (1991).

[10] C. W. McCurdy, D. A. Horner, T. N. Rescigno, and F. Martín, Phys. Rev. A **69**, 032707 (2004).

[11] M. Walter and J. Briggs, J. Phys. B **32**, 1630 (2000).

[12] M. Walter and J. Briggs, J. Phys. B **32**, 2487 (1999).

[13] A. S. Kheifets, Phys. Rev. A **71**, 022704 (2005).

[14] T. J. Reddish and J. M. Feagin, J. Phys. B **32**, 2473 (1999).

[15] D. P. Seccombe *et al.*, J. Phys. B **35**, 3767 (2002).

[16] J. Colgan, M. S. Pindzola, and F. Robicheaux, J. Phys. B **37**, L377 (2004).

[17] W. Vanroose, F. Martín, T. N. Rescigno, and C. W. McCurdy, Phys. Rev. A **70**, 050703(R) (2004).

[18] W. Vanroose, F. Martín, T. N. Rescigno, and C. W. McCurdy, Science **310**, 1787 (2005).

[19] C. W. McCurdy, M. Baertschy, and T. N. Rescigno, J. Phys. B **37**, R137 (2004).

[20] B. Simon, Phys. Lett. A **71**, 211 (1979).

[21] C. A. Nicolaides and D. R. Beck, Phys. Lett. A **65**, 11 (1978).

[22] C. W. McCurdy, D. A. Horner, and T. N. Rescigno, Phys. Rev. A **63**, 022711 (2001).

[23] T. N. Rescigno, M. Baertschy, and C. W. McCurdy, Phys. Rev. A **68**, 020701(R) (2003).

[24] U. Fano, Rep. Prog. Phys. **46**, 97 (1983).

[25] M. E. Rose, *Multipole Fields* (John Wiley and Sons, New York, 1955), pp. 24–28.

[26] D. M. Chase, Phys. Rev. **104**, 838 (1956).

[27] M. Shugard and A. U. Hazi, Phys. Rev. A **12**, 1895 (1975).

[28] M. A. Morrison, M. Abdolsalami, and B. K. Elza, Phys. Rev. A **43**, 3440 (1991).

[29] T. N. Rescigno, B. K. Elza, and B. H. Lengsfield, J. Phys. B

[30] I. Sánchez and F. Martín, Phys. Rev. A **57**, 1006 (1998).

[31] D. T. Stibbe and J. Tennyson, New J. Phys. **1**, 2.1 (1998).

[32] C. W. McCurdy and F. Martín, J. Phys. B **37**, 917 (2004).

[33] F. Martín, J. Phys. B **32**, R197 (1999).

[34] H. Bachau, E. Cormier, P. Decleva, J. E. Hansen, and F. Martín, Rep. Prog. Phys. **64**, 1815 (2001).

[35] D. A. Horner, J. Colgan, F. Martín, C. W. McCurdy, M. S. Pindzola, and T. N. Rescigno, Phys. Rev. A **70**, 064701 (2004).

[36] T. N. Rescigno and C. W. McCurdy, Phys. Rev. A **62**, 032706 (2000).

[37] C. de Boor, *A Practical Guide to Splines* (Springer, New York, 1978).

[38] D. E. Manolopoulos and R. E. Wyatt, Chem. Phys. Lett. **152**, 23 (1988).

[39] M. Baertschy and X. Li, *Proceedings of the 2001 ACM/IEEE Conference on Supercomputing* (ACM, New York, 2001), p. 47.

[40] H. van der Vorst, *Iterative Krylov Methods for Large Linear Systems* (Cambridge University Press, Cambridge, 2003).

[41] Y. Saad, *Iterative Methods for Sparse Linear Systems* (SIAM, Philadelphia, 2003).

[42] H. Kossmann, O. Schwarzkopf, B. Kämmerling, and V. Schmidt, Phys. Rev. Lett. **63**, 2040 (1989).

[43] Th. Weber (private communication).

26, L567 (1993).